Chapter 1 Introduction

The pyramid-like structures on III-V compound semiconductors surfaces have been widely discussed. These structures are formed spontaneously[1-6] or artificially[7-12], and they all have particular optical and electrical properties. For example, some researches have studied the emission characteristics on artificial pyramid-like structures[7-11] with the aid of spatial resolution spectrum, and results showed that the emission on apex and sidewall are quite different. In addition to the optical property, the electrical characteristics were also studied, such as field emission property, that showed good stability as the emitter. Besides the artificial pyramid-like structures, other studies focused on the spontaneously-formed pyramid-like structures, including the formation mechanism[13-16], the optical properties[17-19], and the electrical properties[20].

In this thesis, we studied two types of hillocks on the $Al_xGa_{1-x}N$ (x=0.12) thin film with different morphology. We utilized atomic force microscopy (AFM) and the scanning electron microscopy (SEM) to characterize the structure profile and morphology. Through the measurements of micro- photoluminescence (μ-PL) and micro-Raman (μ-Raman) spectra, we investigated the optical characteristics of the hexagonal hillock structures on $Al_xGa_{1-x}N$ thin film. Finally, we carried

out the composition analysis by using the energy dispersive x-ray spectrometer (EDX) to verify our interpretation of the spectra.

There are five chapters in the thesis, including this chapter " Introduction ". In chapter 2, we briefly describe the structure, optical transitions, and Raman scattering of Ⅲ-Nitride semiconductors. In chapter 3, we give details of the sample preparation, the experimental setup and operation procedures. In chapter 4, we show the results of the surface morphology, photo-luminescence, Raman scattering, and EDX measurements of hillocks and discuss these features in the context of compositional variation. Finally, in chapter 5, we summarize the presently available data and propose a reasonable explanation for the observed transitions.

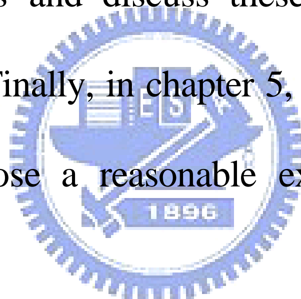

Chapter 2 Theoretical Backgrounds

2-1 Wurtzite Structure and Related Raman Tensor

The wurtzite structure is similar to the basic zinc-blende (ZB) structure as shown in Fig. 2-1-1, each group-Ⅲ atom is coordinated by four nitrogen atoms. Alternatively, each nitrogen is also coordinated by four group-Ⅲ atoms (like a tetrahedron). The main difference between these two structures is in the stacking sequence of the closest packed diatomic planes, the stacking sequence is ABABAB··· in the <0001> direction for the wurtzite structure, and ABCABC··· in the <111> direction for the ZB structure. Therefore, the phonon dispersion curves for the wurtzite may be deduced from those for the ZB by folding the Brillouin Zone (BZ) along the ? (111) direction. Group theory (i.e. the point group C_{6v}) predicts the following irreducible representations at the G-point for the wurtzite structure in BZ :

$$\Gamma = 2(A_1(R_p, I_r) + E_1(R_p, I_r) + E_2(R_d) + B_1(ia))$$

Among these, one A_1 and one E_1 are acoustic vibration while the B_1 mode is silent. The E_2 modes are Raman-active, the A_1 and the E_1 modes are both Raman and infrared active. Concerning the polar modes (A_1 and E_1), they are split into the LO and TO modes due to the long range Coulomb field, so that there are six Raman-active phonons.

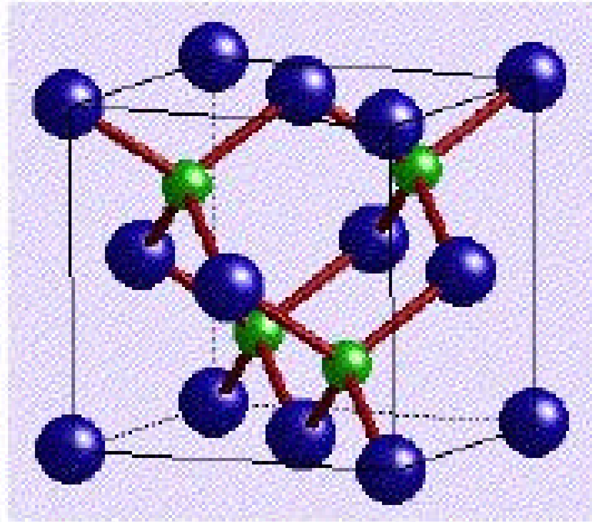

(a) The Zinc-Blende structure

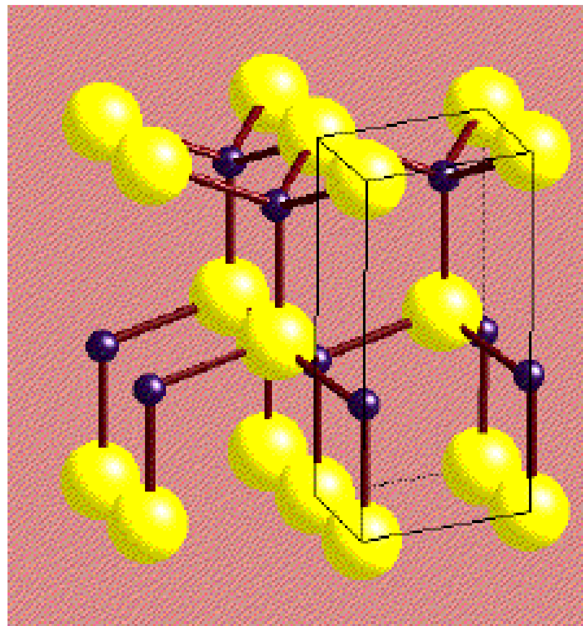

(b) The Wurtzite structure

http://www.univ-lemans.fr

Fig. 2-1-1 The common structures of Ⅲ-Ⅴ compound semiconductors

However, for non-polar modes (E_2 and B_1), which can be associated with the back-folded BZ edge at X point of the corresponding ZB structure, Al, Ga and N atoms vibrate in anti-parallel directions. The two E_2 non-polar normal modes can couple to each other, since they belong to the same representation of the C_{6v} group.

The Raman tensors for the C_{6v} point group are expressed by the susceptibility matrix $\overleftrightarrow{\boldsymbol{c}}$ in the following forms:

$$A_1 \text{ mode } \begin{bmatrix} a & 0 & 0 \\ 0 & a & 0 \\ 0 & 0 & b \end{bmatrix}$$

$$E_1 \text{ mode } \begin{bmatrix} 0 & 0 & c \\ 0 & 0 & 0 \\ c & 0 & 0 \end{bmatrix} \text{ and } \begin{bmatrix} 0 & 0 & 0 \\ 0 & 0 & c \\ 0 & c & 0 \end{bmatrix}$$

$$E_2 \text{ mode } \begin{bmatrix} d & 0 & 0 \\ 0 & -d & 0 \\ 0 & 0 & 0 \end{bmatrix} \text{ and } \begin{bmatrix} 0 & -d & 0 \\ -d & 0 & 0 \\ 0 & 0 & 0 \end{bmatrix}$$

The scattering probability is formed by taking the product of the susceptibility matrix $\overleftrightarrow{\boldsymbol{c}}$ with the incident $\vec{\boldsymbol{e}}_i$ and scattered $\vec{\boldsymbol{e}}_s$ polarization vectors in the form $\left|\vec{\boldsymbol{e}}_i \cdot \overleftrightarrow{\boldsymbol{c}} \cdot \vec{\boldsymbol{e}}_s\right|$. It is non-zero for Raman active modes with particular combinations of $\vec{\boldsymbol{e}}_i$ and $\vec{\boldsymbol{e}}_s$. By using the tensor calculation, the Raman selection rules of the hexagonal Ⅲ-N are shown in the Table 2-1-1.

Phonon modes / Polarization configuration	A_1	E_1	E_2
$z(yy)\bar{z}$	a^2	0	d^2
$z(yx)\bar{z}$	0	0	d^2
$y(xx)\bar{y}$	a^2	0	d^2
$y(xz)\bar{y}$	0	c^2	d^2
$z(\overline{yy})\bar{z}$	a^2	0	d^2
$z(\overline{yx})\bar{z}$	0	0	d^2

The table was calculated from the susceptibility and the incident and scattered polarization vectors.

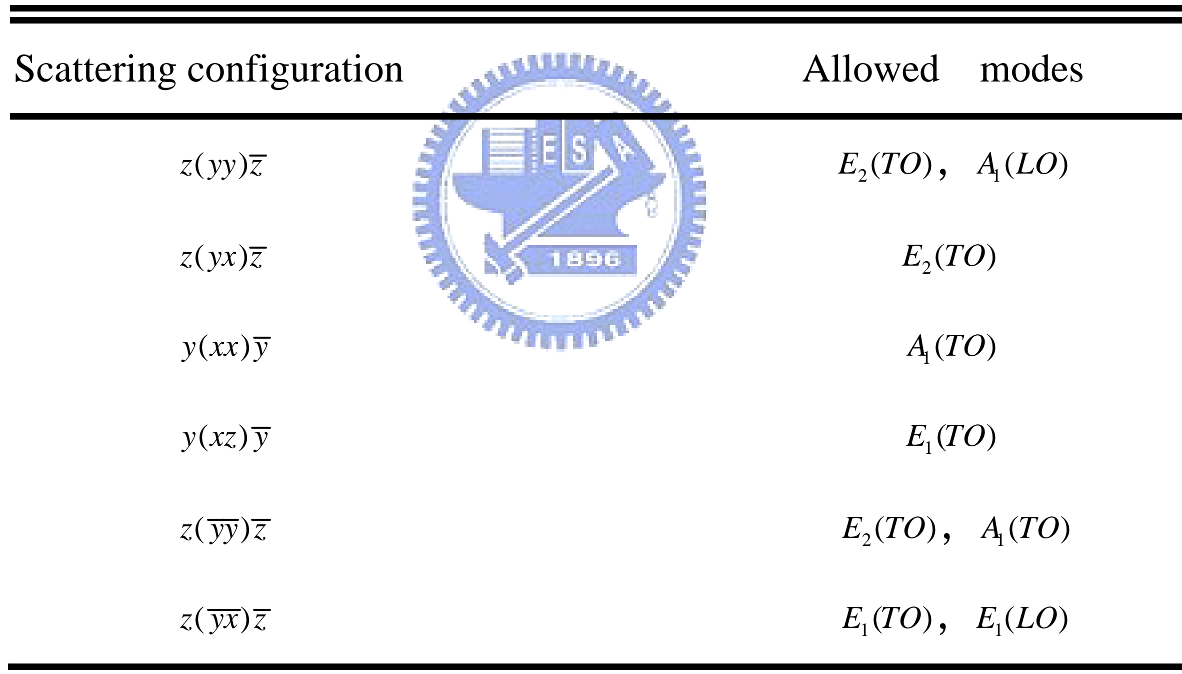

Scattering configuration	Allowed modes
$z(yy)\bar{z}$	$E_2(TO)$, $A_1(LO)$
$z(yx)\bar{z}$	$E_2(TO)$
$y(xx)\bar{y}$	$A_1(TO)$
$y(xz)\bar{y}$	$E_1(TO)$
$z(\overline{yy})\bar{z}$	$E_2(TO)$, $A_1(TO)$
$z(\overline{yx})\bar{z}$	$E_1(TO)$, $E_1(LO)$

Raman selection rules for optical phonons in wurtzite crystal.

Table 2-1-1 The selection rule for hexagonal structures.

2-2 Photoluminescence in Semiconductors

As the laser beam irradiates a semiconductor, electrons and holes can be created if the photon energy is larger than the semiconductor band gap. The electrons and holes may be scattered and then redistribute near the conduction band minimum and the valence band maximum, through the process called " Thermalization ". Under the quasi-thermal equilibrium, electrons and holes may recombine and produce photons. If the defects or impurities exist in the semiconductors, the electron-hole pairs may recombine and create photons via the levels formed by defects and impurities, these levels are often called "radiative centers". Furthermore, defects and impurities may also create " non-radiative centers ", at which the electron-hole pairs are absorbed but do not emit photons, so that the emission efficiency will be reduced. Two types of recombination are described as follows :

(A) Radiative Transition

(I) Band to Band Transition

In perfect semiconductors, the excited electrons and holes will accumulate at the conduction band and valence band extrema. As shown in Fig. 2-2-1, electron-hole (e-h) pairs will recombine radiatively with high probability (in the direct band gap semiconductor). The

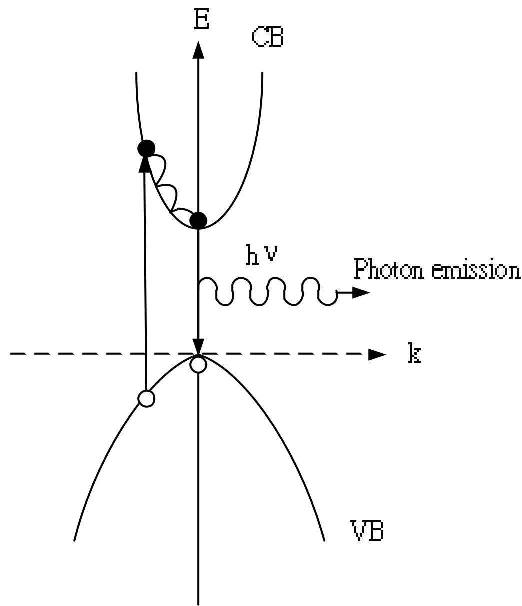

(a) Direct transition

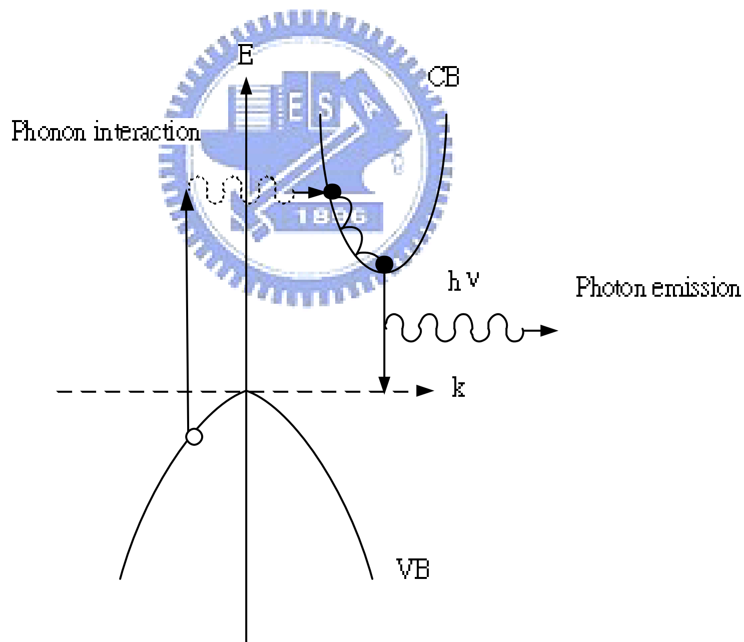

(b) Indirect transition

Fig. 2-2-1 The schematic representation of direct and indirect transitions.

recombination rate can be expressed as :

$$R = \int R(h\mathbf{n})d(h\mathbf{n}) \sim np$$

the rate is proportional to the electron-hole concentration. But in the indirect band gap semiconductors, the transition must involve an additional particle – "phonon" (in order to satisfy the momentum conservation rule). Thus, the transition probability will be reduced, and the emission efficiency is lower than the direct band gap semiconductors. Most of Ⅲ-Nitrides (such as GaN、InGaN、AlGaN) are the direct band gap semiconductors. In our studies, we observed the band-to-band transition of AlGaN.

(II) Exciton Transition

In high quality semiconductors, the Coulomb interaction between the conduction band electrons and the valence band holes will result in the formation of the bound electron-hole pairs, that is the so called " exciton ", as shown in Fig. 2-2-2. The exciton is analogous to "positronium atom" – an electron bound to a positron, and this quasi-particle (exciton) is electrically neutral. In most Ⅱ-Ⅳ、Ⅲ-Ⅴ semiconductors, the exciton radius (Bohr radius) is large in comparison with the length of the lattice unit cells, they are called " Wannier excitons ". Beside this, if the radius of the excitons is on the order of or

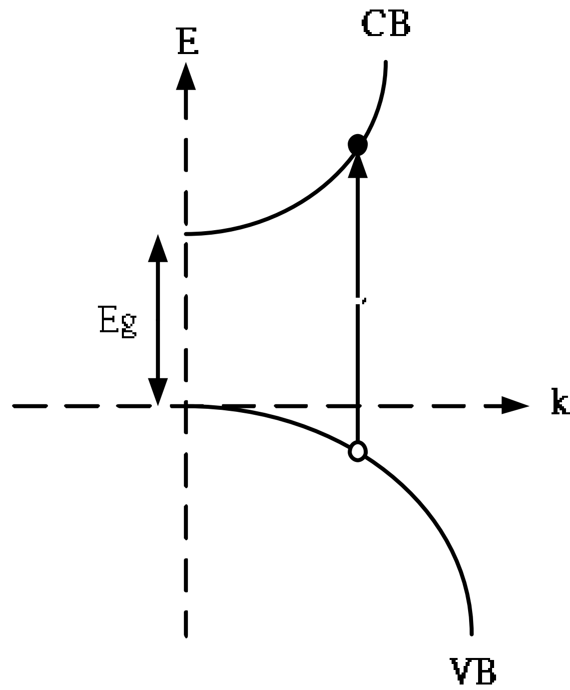

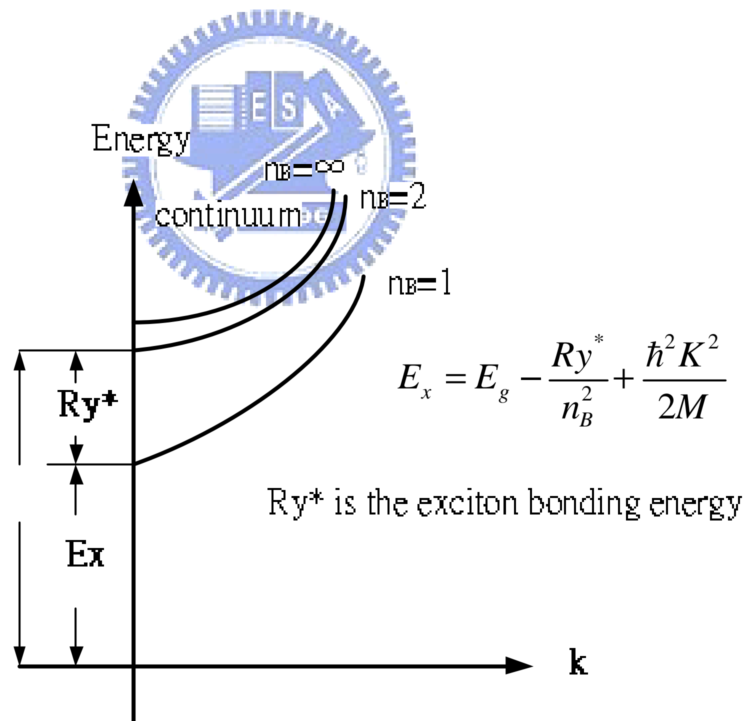

Fig. 2-2-2 A pair excitation in the scheme of valence and conduction band in the exciton energy diagram for a direct semiconductor

smaller than an atomic unit cell, these are called “ Frenkel excitons ”. In order to obtain the exciton’s energy levels, one may write the linear combination of electron and hole Bloch functions as follows:

$$\psi(r_e, r_h) = \sum \phi(\vec{k}_e, \vec{k}_h) \cdot \varphi_{c,\vec{k}_e}(\vec{r}_e) \cdot \varphi_{v,\vec{k}_h}(\vec{r}_h)$$

where $\phi(\vec{k}_e, \vec{k}_h)$ is the expansion coefficient, $\varphi_{c,\vec{k}_e}(\vec{r}_e)$ is the Bloch function for an electron in the conduction band with wave vector $\vec{k}_e$ at position $\vec{r}_e$, and $\varphi_{v,\vec{k}_h}(\vec{r}_h)$ represents the the Bloch wave function for a hole in the valence band with wave vector $\vec{k}_h$ at position $\vec{r}_h$. By inserting these functions into the two-particle *Schrödinger* equation :

$$\left(-\frac{\hbar^2}{2m_e}\nabla_e^2 - \frac{\hbar^2}{2m_h}\nabla_h^2 - \frac{e^2}{\varepsilon_0\left|\vec{r}_e - \vec{r}_h\right|}\right) \cdot \psi(r_e, r_h) = E\psi(r_e, r_h)$$

one may get the exciton’s eigen-energy (total exciton energy with a principal quantum number “n”) as :

$$E_n = E_g - \frac{\hbar^2}{2m_r a_B^2} \cdot \frac{1}{n^2} + \frac{\hbar^2 K_c^2}{2M}$$

where E_g is the energy gap of semiconductor , the second term exhibits the exciton’s energy levels with the exciton Bohr radius $a_B = \frac{\varepsilon_0 \hbar^2}{m_r e^2}$, the last term is the center-of-mass energy. m_r and M are the reduced mass and the total mass, respectively. So the exciton may dissociate into a free

electron-hole pair and recombine with the photon energy :

$$h\nu = E_g - \frac{m_r^2 e^4}{2\varepsilon_0^2 \hbar^2} \cdot \frac{1}{n^2}$$

In our previous studies, the additional transition line was attributed to the localized excitons.

(III) Donor Acceptor Pair Recombination (DAP)

The impurities present in the semiconductors may form the donor (positive) or the acceptor (negative) levels in the energy gap. The electrons and holes created by the laser excitation may be bound to the donor (D^+) and the acceptor (A^-) to form the neutral donor (D^0) and acceptor (A^0). If the neutral donor electron and the acceptor hole recombine, as expressed by :

$$D^0 + A^0 \rightarrow h\nu + D^+ + A^-$$

it can emit photon with an energy :

$$E_{DAP} = h\nu = E_g - (E_D + E_A) + \frac{e^2}{\varepsilon \cdot R_{DA}}$$

where E_g is the energy gap of semiconductor, E_D and E_A is the binding energy for the electron to the donor and the hole to the acceptor. R_{DA} is the distance between the donor and the acceptor. If the R_{DA} increases, the transition probability will reduce, so does the PL intensity.

(B) Non-Radiative Transition

There are several transitions that compete with the radiative transition and thus reduce the emission efficiency. They are described as follows :

(I) The e-h pair is scattered by the phonon or carriers and loses its energy.

(II) The e-h pair recombines at defect, dislocation, grain boundary or surface, and loses its excess energy, the so-called “cascade process”.

(III) The e-h pair loses its energy via the “ Auger process ” that involves the core level transitions.

All the non-radiation transitions will compete with radiation transitions, the more the non-radiation transition, the lower the PL intensity.

2-3 Raman scattering

Photons may be scattered inelastically by the optical and acoustic phonons, when an optical phonon was involved in the scattering, the process is called the Raman scattering. This effect was firstly discovered by Sir C.V. Raman in the molecular light scattering. The photon frequenncy is shifted after interacting with a phonon. If the phonon creates in the interaction, the photon energy would be shifted toward lower frequency, the so called "Stokes process". On the other hand, if the phonon is absorbed in the interaction, the photon energy would be shifted toward higher frequency, it is the "Anti-Stokes process". All these processes must obey the energy and the momentum, conservation laws.

$$\hbar\omega_R = \hbar\omega_i \pm \hbar\Omega_{phonon}$$

$$\vec{k}_R = \vec{k}_i \pm \vec{k}_{phonon}$$

where $\hbar\omega_R$ and $\vec{k}_R$ are the scattered photon energy and momentum, $\hbar\omega_i$ and $\vec{k}_i$ are the incident photon energy and momentum, $\hbar\Omega_{phonon}$ and $\vec{k}_{phonon}$ are the phonon energy and momentum, respectively. Because the phonon frequency can be expressed as[36] :

$$\Omega(\vec{k})_{phonon} = \sqrt{\frac{\lambda(\vec{k})}{M}}$$

where $\lambda(\vec{k})$ is the force constant with wave vector $\vec{k}$ and $\vec{k}$ is a function of lattice constant. If the strain or the composition changes, the

lattice constant will also change and affect the phonon frequency. According to the shift of the phonon frequency, we may analyze the crystalline structure.

From the scattered photons, one may obtain a lot of information about the semiconductor structure, orientation, symmetry, even the doping concentration via the scattered Raman intensity, shift, linewidth, and the line shape.

2-4 Scanning electron microscopy (SEM) and Energy dispersive x-ray spectrometer (EDX)

In optical microscopy, we obtain the magnified morphology of the sample via the photon collected by the lens. But in electron microscopy, the electron is accelerated by the high voltage, then the electron beam is converged and focused by the electric-magnetic lens. The beam would scan over the sample by the scanning coil, when the electron beam strikes the sample, one obtains the electron signals. As the electron beam scans over the sample, the electron signals from each region are recorded, and one can get the sample morphology through calculation.

When the electron beam strikes the sample, secondary electrons、backscattered electrons、Auger electrons、x-ray、cathodoluminescence etc. would be excited. For the image, we operated at the " Secondary Electron Image " (SEI) or " Backscattered electron image " (BEI) modes, that were described as the following:

(I) Secondary Electron

When the atoms on the surface are collided by the incident electrons, the weak-bonding electrons would be released, electrons' energy were lowered by 50eV, they are called secondary electrons. Because low-energy electrons are created only near the surface, these are sensitive

to the changes of the surface, so one can get high spatially-resolved images.

(II) Backscattered Electron

When the incident electrons are collided with the atoms elastically, the electrons escape from the surface with the same or less energy, these electrons are called backscattered electrons. The number of scattered electrons changes with different elements, when the atomic number of the element increases, the backscattered electrons would increase, so the region with higher atomic number would become brighter on the image. It can be utilized for the atomic qualitative analysis. But the scattered electrons come from the deeper region, so the electron beam was scattered more dispersively, and the spatial resolution is worse than secondary electron mode.

When the focused electron beam strikes the sample, the x-ray would also emit. Because each element has its characteristic x-ray line, we can analyze the peak position to resolve the element. The x-ray can excite the electrons and holes in the detector, so that the carriers would contribute to the electrical pulse. We may transfer the signals into the multi-channel analyzer and plot the spectrum for analyzing the element. The processes are described as follows:

(1) Find the element that we want to analyze using a standard sample

(2) Under the same conditions, record the peak position of the characteristic x-ray from the standard sample and our sample.

The background intensity of the standard sample is needed, too.

(3) Correct the " dead time " of the system to get the peak intensity.

(4) Get the net intensity by subtracting the background intensity:

$$C_i^{unk} \approx K_i^{unk} = \frac{I_i^{unk}}{I_i^{STD}}$$

for C_i^{unk} ：the weight ratio of element i in our sample,

K_i^{unk} ：relative peak intensity of the element i,

I_i^{unk} ：net peak intensity of the element i in our sample,

I_i^{STD} ：peak intensity of the standard sample,

and "unk" means unknown sample.

Chapter 3 Experiments

3-1 Sample preparation

The $Al_xGa_{1-x}N$ thin film sample, obtained from the "Chung-Shan Institute of Science and Technology ", was grown by the Low Pressure Metalorganic Chemical Vapor Deposition (MOCVD) system. The system (AIXTRON 200) was equipped the horizontal quartz reactor, with the radio- frequency (RF) as the heating source. The $Al_xGa_{1-x}N$ thin film was deposited on the (0001) sapphire, by using Trimethylgallium (TMGa) 、Trimethylaluminum (TMAl)、Ammonia (NH_3) as the Ga、Al、N sources, and the high- purity H_2 as the carrier gas. Prior to growth, the substrate was sent to the reactor and thermally cleaned under the hydrogen ambient at 1120 ℃ for 10 minutes. In order to minimize the lattice mismatch between the thin film and sapphire, we deposited an aluminum nitride (AlN) buffer layer about 25nm and then aluminum gallium nitride ($Al_xGa_{1-x}N$) thin film about 0.7 µm.

3-2 Atomic Force Microscopy (AFM)

The basic operational principle of atomic force microscopy is to bias the cantilever with AC and DC voltages, when the AC signal was tuned to the resonance frequency of the cantilever, the cantilever will vibrate at larger and clearer amplitude. One may move the probe with sharp tip on the cantilever to the sample surface. If the distance between the tip and the sample is reduced, the attractive and repulsive forces will make effects on the probe, that may change the amplitude or the displacement of the cantilever. Then, one may direct the laser spot on the cantilever, and detect the reflective signals from the cantilever. From the reflective signals, we may analyze the sample surface. Traditionally, one may operate the AFM system in three modes to obtain the sample morphology. We introduce these modes as follows, with the diagrams shown in Fig. 3-2-1. In our experiment, we operated the AFM in semi-contact mode.

(I) Contact Mode

In this mode , the cantilevers touches the surface and scans over the sample. Via the electrical feedback loop, the piezoelectric scanner enforces the cantilever with a constant force. As the surface height changes, the system will detect the deflection signals of the cantilever and then it modulates the scanner's height to keep the constant force

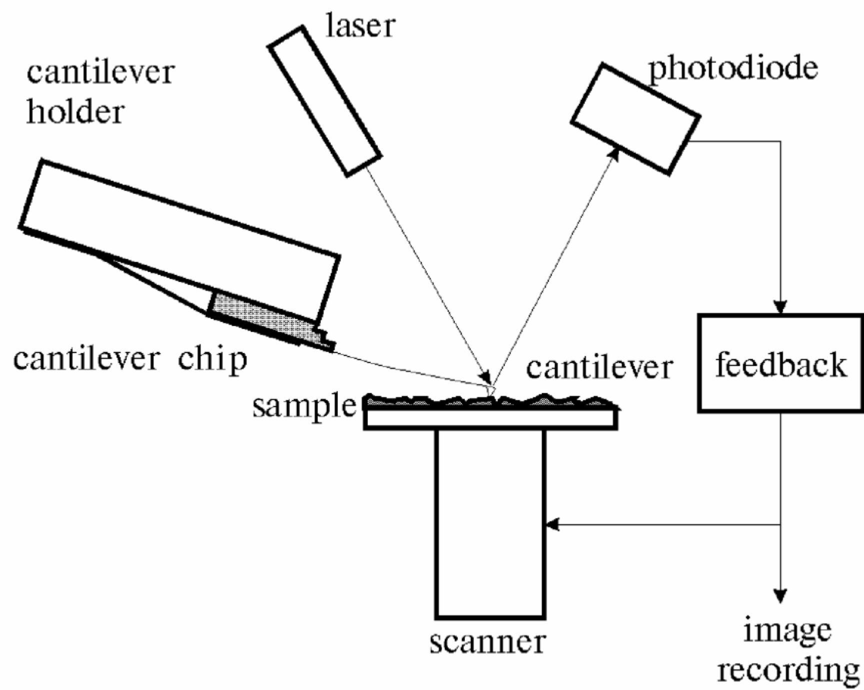

The diagram shows the operation of the AFM system

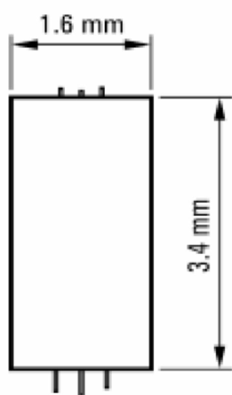

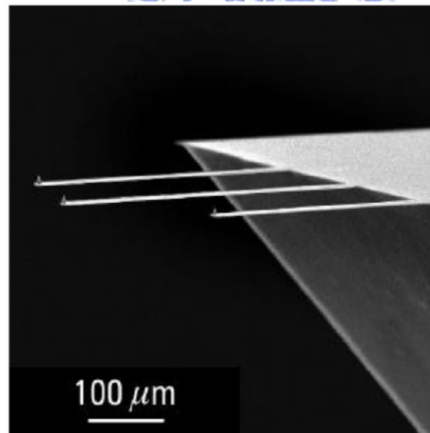

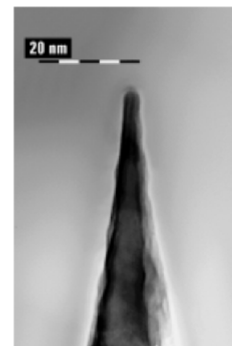

Probe chip Cantilever of the probe Tip

Fig. 3-2-1 AFM system and Probe

condition. The modulation of the scanner's height will be recorded and processed by the controller and the software, and finally provides us with the sample's morphology.

(II) Non-Contact Mode

In order to avoid the destruction from the probes, non-contact mode is preferred. It vibrates with a small amplitude and utilizes the long range Van der Waal's force between the tip and sample. But the long range force is not sensitive to the changes of the height, it needs advanced modulation technology to enhance the signal to noise ration (S/N). In the ambient environment, the non-contact mode's resolution is only about 50nm. If we want to obtain the better images, the system must be loaded into the vacuum chambers.

(III) Semi-Contact Mode

The semi-contact mode is improved from the non-contact mode, the amplitude of the cantilever is enlarged , and the height between the tip and the sample is reduced. Through the special modulation technology, the changes of surface height affecting the cantilever's amplitude may be recorded, and one may obtain the morphology through the software analysis. It is also more sensitive to interact with surface, that is more suitable to characterize the surface distribution of the magnetic and

electric filed、elasticity and viscosity.

Beside the morphology measurements, the AFM system can also be utilized for other researches, such as the micro I-V measurements, spreading resistance distribution, or the nano-lithography. All the new functions are still under developing.

Our Scanning Probe microscopy (SPM) system was manufactured by the " Molecular Devices and Tools for Nano Technology " (NT-MDT) in Russia. The AFM system we used was Solver P47H, that can be operated in multi-modes, such as AFM for morphology measurements, lateral force microscopy for the friction distribution, and MFM, EFM, SKM, etc. In this study, we obtained the hillock's profile from the AFM system which can be operated in contact mode, non-contact mode, and semi-contact modes. In order to obtain the better images, we utilized the semi-contact mode to obtain the morphology. The AFM probes were also from the NT-MDT. They have a cantilever about 50 or 80 μm, and a sharp tip with a radius of curvature about 10 nm.

3-3 Micro-PL system

The Micro-PL system incorporated an Olympus BH2 optical microscope. The system is shown in Fig. 3-3-1. The He-Cd laser operated at 325nm (Omnichrome 2074-M-A02) is the light source. The beam was reflected by an UV mirror and then incident into the microscope, passing through a beam splitter and focused by the near-UV objective lens sets (Mitutoyo NUV 100X , N.A.=0.5). The focused spot is detected by a color CCD camera (Sony Exwave HAD), with a diameter ≦ 3 μm. The luminescence signals from the laser beam were collected by the objective lens, then reflected by the beam splitter, through the long pass filter to cut off the laser signals. Finally, the PL signals were sent into the optical fiber, and dispersed by the monochrometor (ARC Pro 500) and detected by the photomultiplier tube (PMT Hamamatsu R955). As the entrance and exit slits of the monochromator were both set to 50 μm, the spectral resolution was about 0.2 nm. All signals were processed by the LabView-based software.

(Micro-Photoluminenscence system)

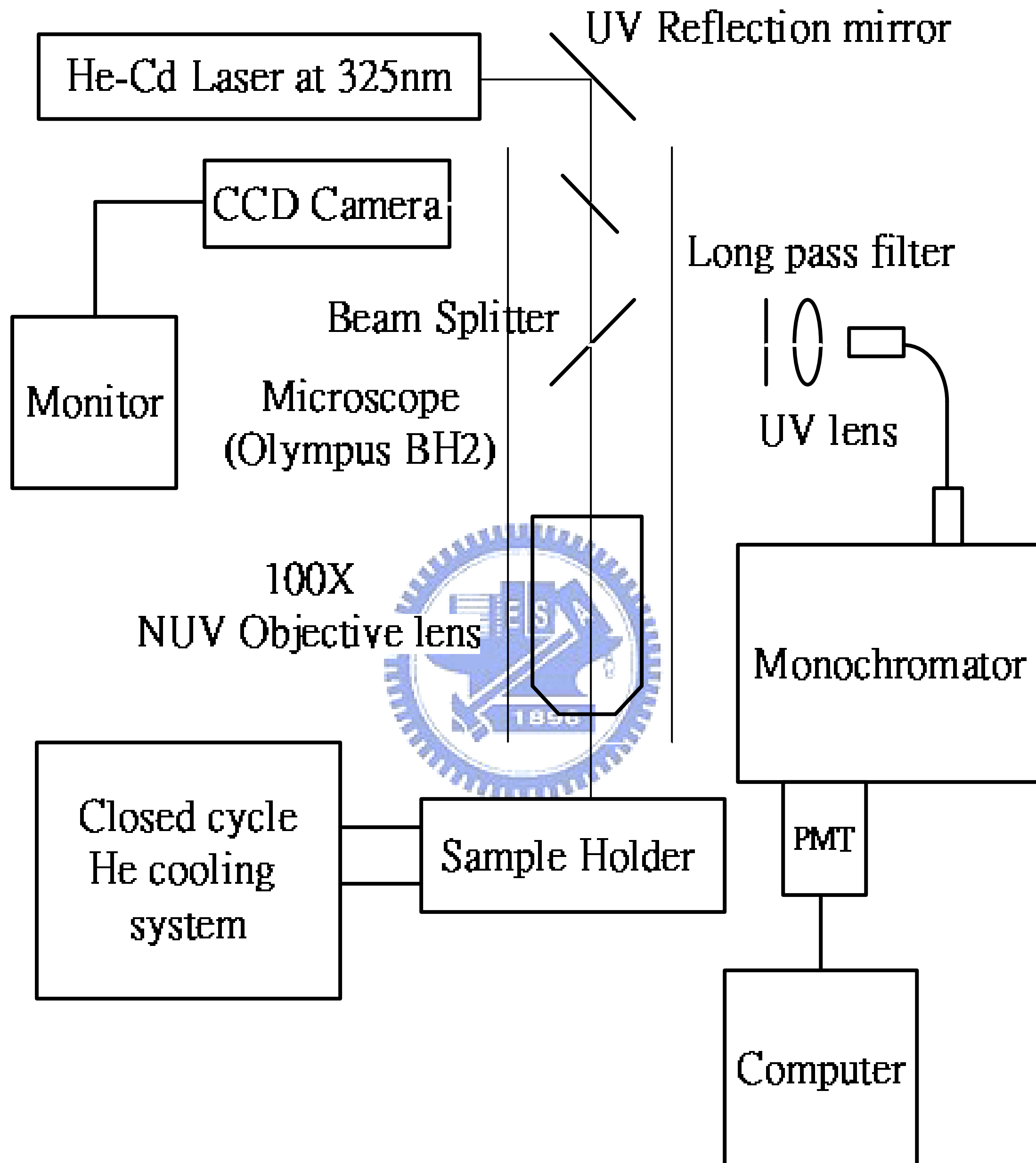

3-4 Micro-Raman system

The HR800 Micro-Raman system was manufactured by Jobin-Yvon corporation. The system is shown in Fig. 3-4-1. It consists of an Olympus BX-41 confocal microscope, a Raman spectrometer, and a liquid nitrogen cooled CCD detector. The laser beam (at 488nm) from the Coherent Innova 90C-A6 multiline visible laser, and reflected by five UV mirrors, and then incident into the system. To cut off the laser plasma line, an inteference filter (at 488 nm) was inserted. After reflecion by a mirror and a notch filter (at 488 nm), the beam was guided into the microscope, and focused by the objective lens (Olympus 100X N.A.= 0.9), with the spot size on the sample about 2 μm. The Raman signals from the sample and the laser signals reflected by the sample were both collected by the objective lens. However, after the notch filter, only the Raman signals passed and were guided into the Raman spectrometer. This Raman spectrometer is equipped with a single grating (2400 g/mm), with the spectral resolution better than 0.4 cm^{-1}. Finally, the dispersed Raman signals will be collected by the CCD detector (UV coating open electrode chip and CCD-3000v controller). All the data were processed by the commercial software ‘Labspec’.

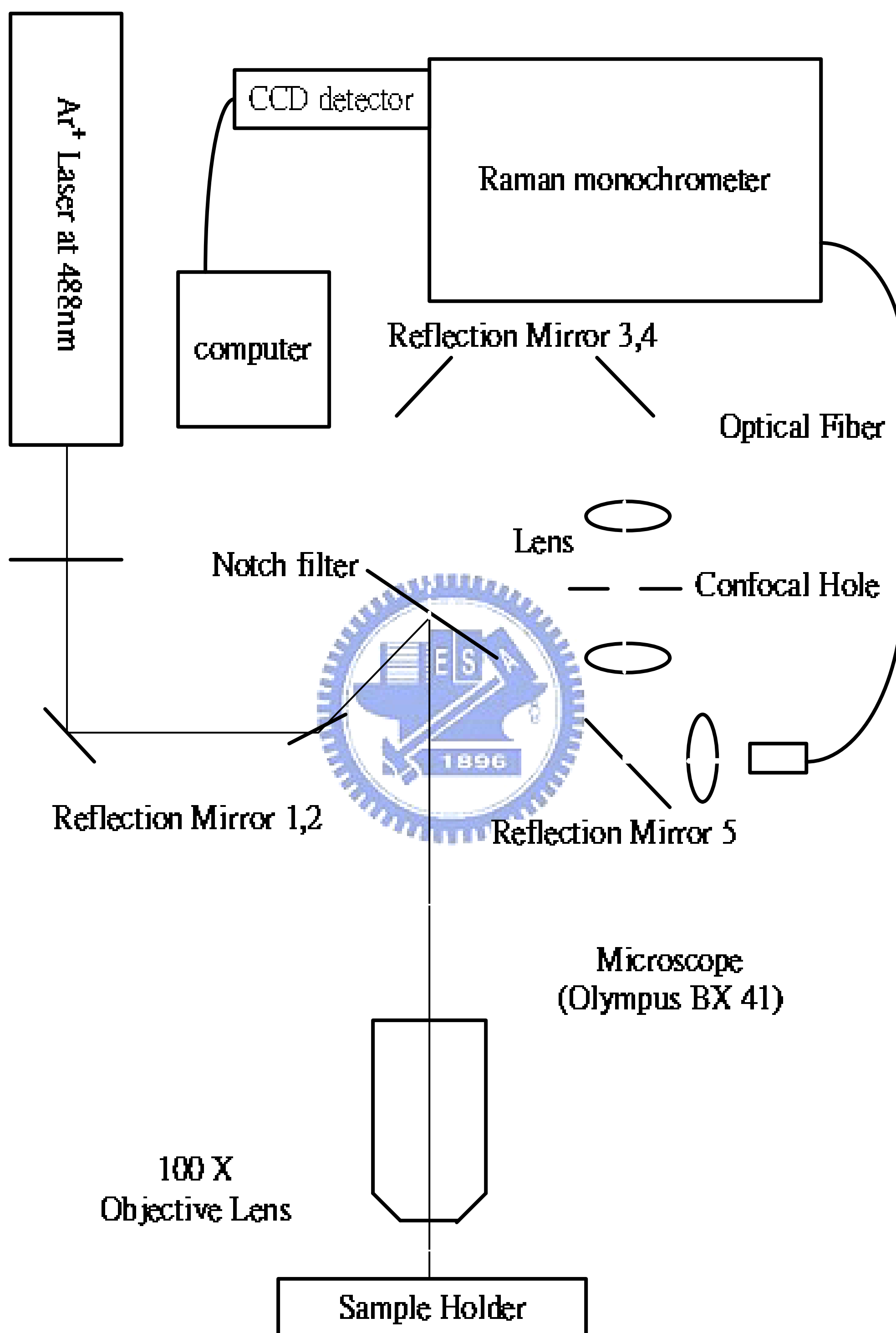
Micro-Raman system
Ar+ Laser at 488nm
CCD detector
Raman monochrometer
computer
Reflection Mirror 3,4
Optical Fiber
Lens
Notch filter
Confocal Hole
Reflection Mirror 1,2
Reflection Mirror 5
Microscope
(Olympus BX 41)
100 X
Objective Lens
Sample Holder

3-5 Field Emission SEM and EDX

In the experiments, we utilized the JSM-6500F field emission SEM manufactured by the Japan Electron Optics Laboratory (JEOL). The electron beam was emitted from the Schottky emitter, which was operated at 1800K. The electrons obtain the thermal energy and jump across the barrier (but not via the tunneling), and then escape from the tip. The spatial resolution is 1.5nm at 15kV and 5nm at 1kV, the magnification is between 10~500,000 X. This SEM is also equipped with the energy dispersive spectrometer manufactured from the Oxford Instrument, it can detect signals of the element with the atomic number between 5~92.

Chapter 4 Results and Discussion

In this chapter, we present experimental results of the pyramid-liked structure – hexagonal hillocks on $Al_xGa_{1-x}N$. The AFM image of the morphology of hillocks, the spatially resolved μ-PL and the μ-Raman spectra are analyzed to elucidate the photo-carriers recombination mechanism and the phonon distribution. The SEM images of hillocks, and the EDX equipped on SEM were measured for qualitative element analysis.

4-1 Morphology of hillocks

As shown in Fig. 4-1-1 and Fig. 4-1-3, the AFM images exhibit the morphology and profile of two types of hillock. The first type looks like a truncated pyramid, it has a quasi-flat top and the angle between the sidewall and plane region is about 55°; the second type looks like a ger, it has two-step sidewall and an obtuse apex, the angle between plane region and bottom sidewall is about 20° while the upper sidewall is about 13°. The significant difference can also be observed in the SEM images of Fig. 4-1-2 and Fig. 4-1-4. Some reports indicated that the control of growth condition[21] will affect the formation shape. And the strain on surface also plays an important role of the pyramid-like structures[13-16].

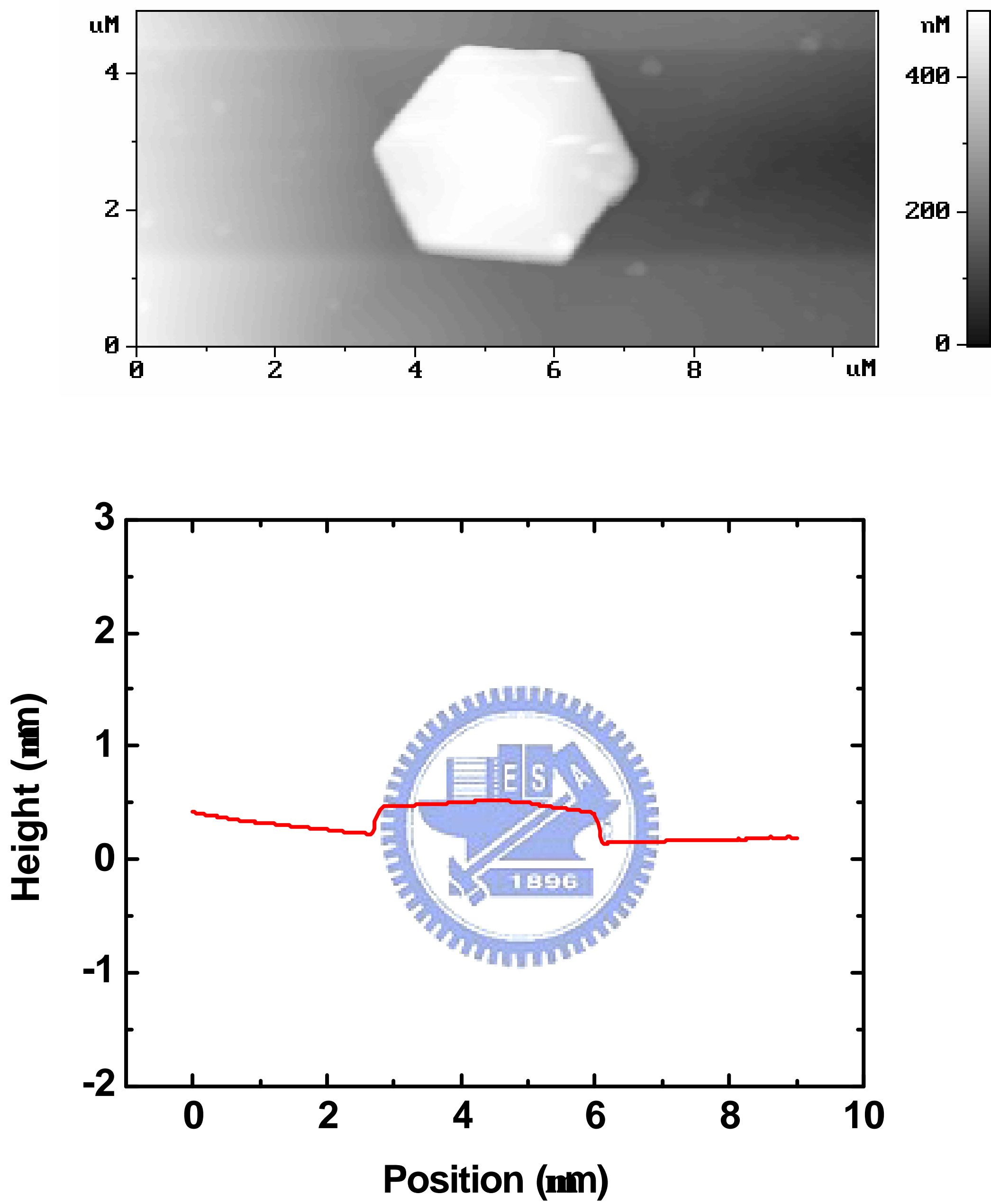

Fig. 4-1-1

AFM image and profile of flat top hillocks

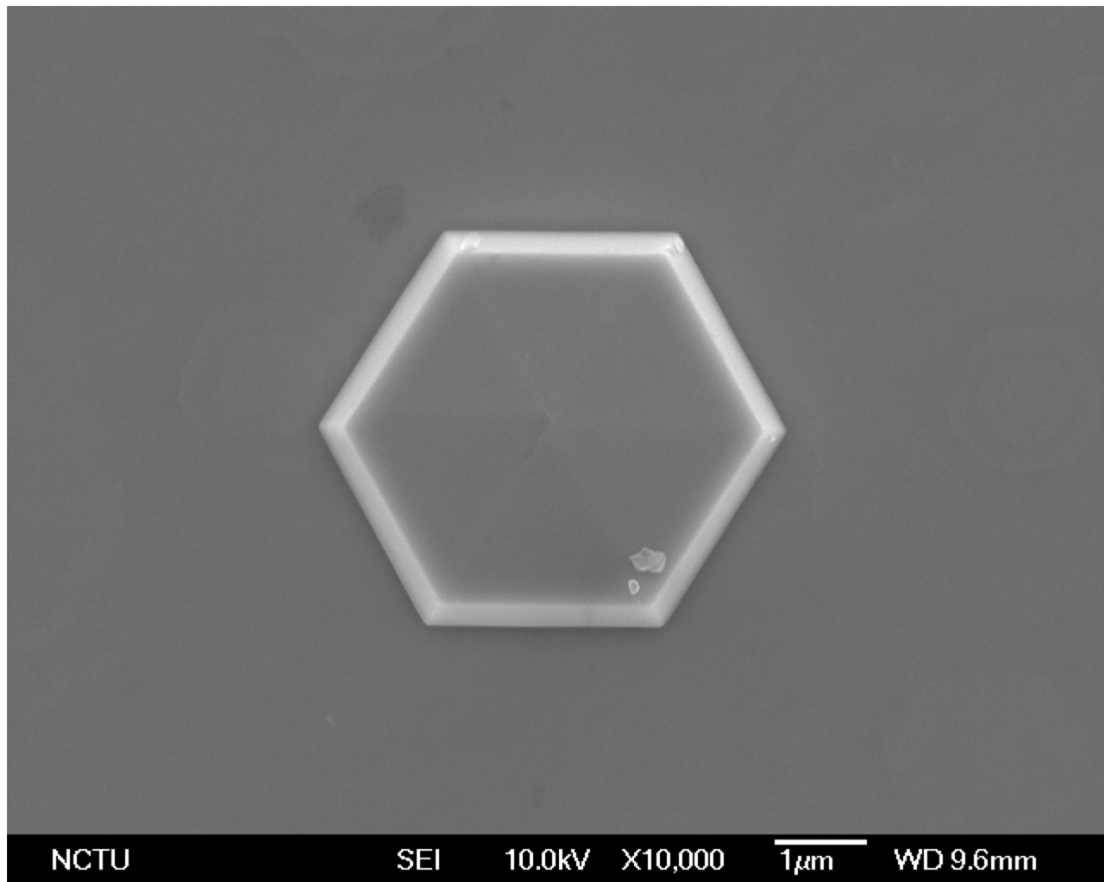

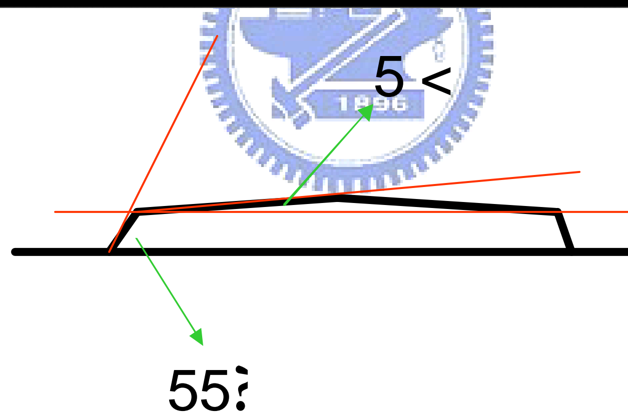

Fig. 4-1-2

SEM image and side view of flat top hillocks

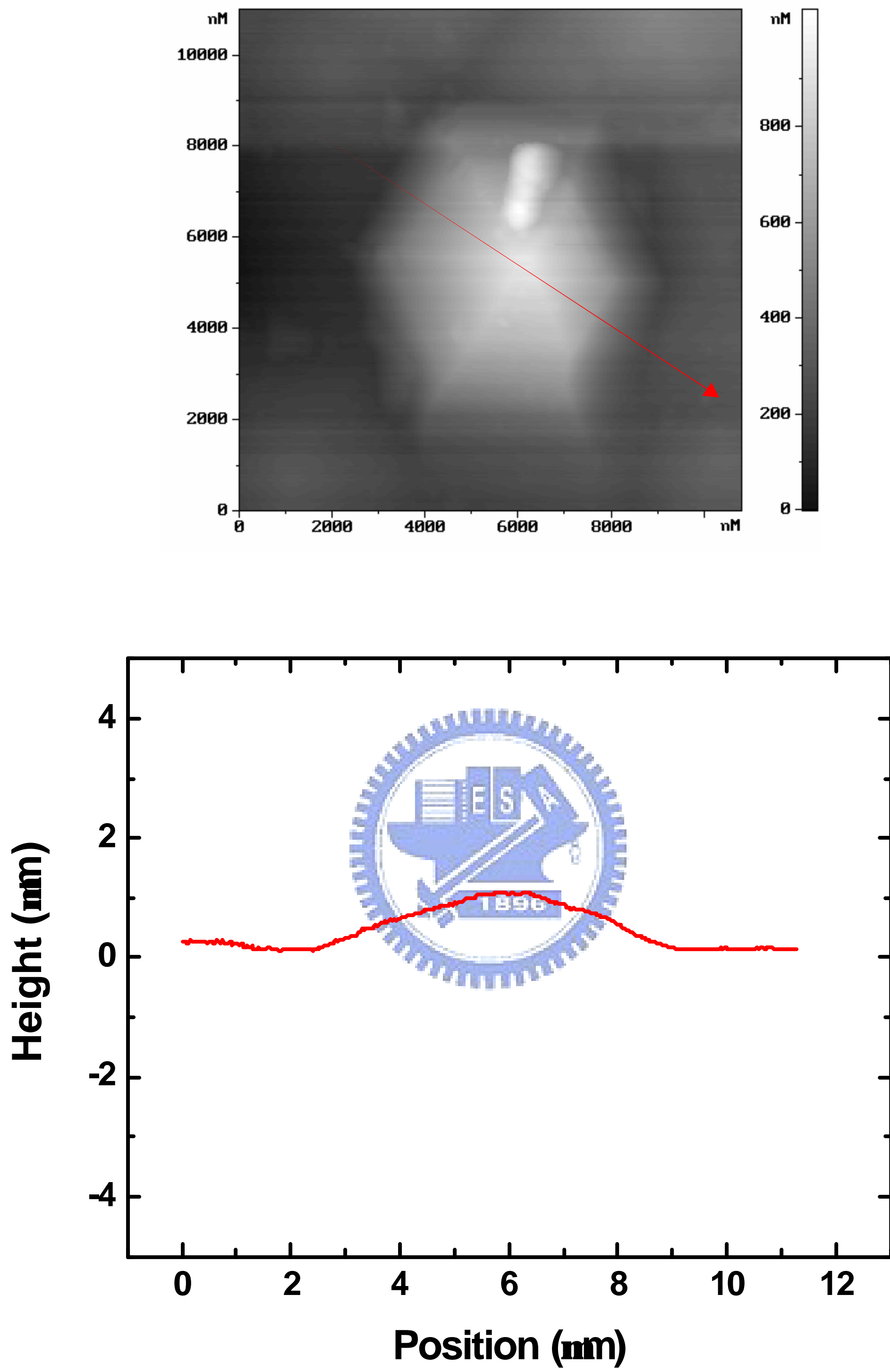

Fig. 4-1-3

AFM image and profile of two step hillocks

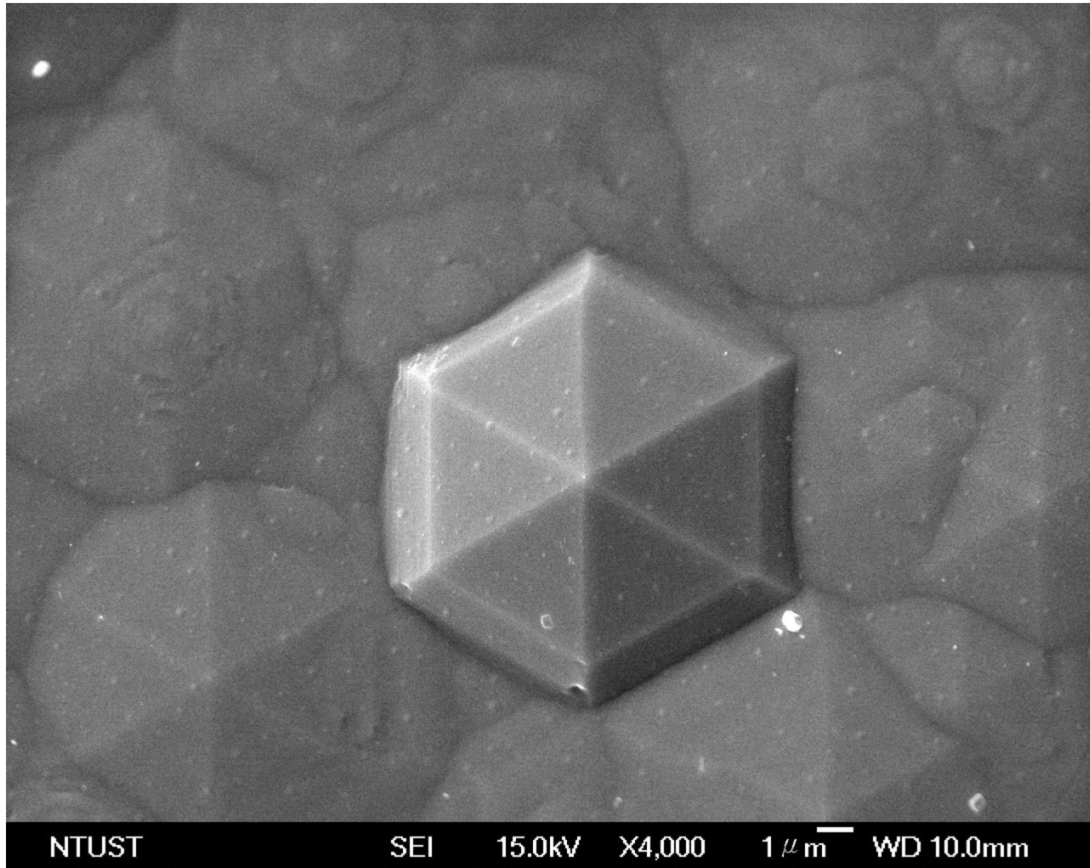

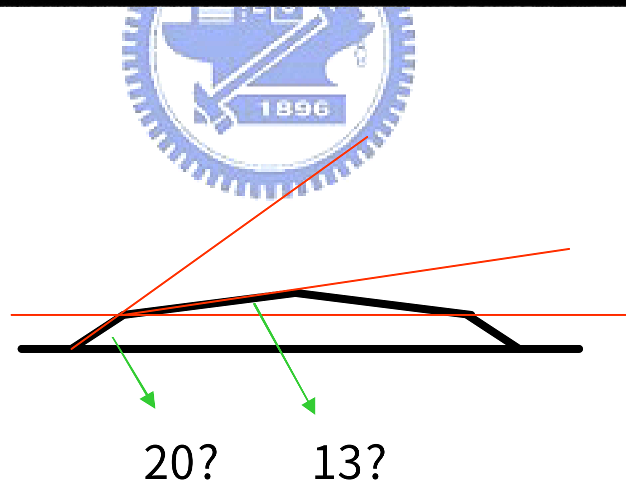

Fig. 4-1-4

SEM image and side view of Two steps hillocks

4-2 Micro-PL spectra of hillocks

To investigate the behavior of photo-excited carriers and recombination mechanisms of hillocks, we show the μ-PL spectra which were taken at different locations across the hillocks and their optical images under the microscope. All spectra were acquired at room temperature, and the spectral resolution is about 0.2nm. In Fig. 4-2-1 and Fig. 4-2-2, we can observe the near-band-edge emission (NBE) at ~340nm (3.6eV) on the plain region and as close to the edge of the flat top hillock. However, we noticed that inside the hillocks, another emission is emerging at ~350 nm (3.5 eV). The near-band-edge emission (~340nm) does not shift, while the extra peak (~350nm) appears only inside the hillock. This extra peak is stronger than the NBE, and belongs only to the hillocks. The main features are also observed in the two step-sidewall hillocks in Fig. 4-2-4 and 4-2-5. This phenomenon had been observed by Robins and Wickenden[17], but they did not provide a clear explanation. Our observation differs from the progressive shift in strained samples[22-23]. Previously, we attributed the emission to the localization effect of some acceptor-like states[24]. From this investigation, we have come up with an alternative interpretation that the emission may be attributed to Al fluctuation.

If the optical properties of the hillock are dominated by the Al fraction fluctuation, we may estimate the Al fraction in the plain region and inside the hillocks. From the μ-PL spectra, the peak position can be converted into photon energy as:

$$E_g(eV) = \frac{1240}{\lambda(nm)}$$

By substituting it into the empirical formula, one obtains Al fraction "*x*" :

$$E_g^{Al_xGa_{1-x}N}(x) = (1-x)\cdot E_g^{GaN} + x\cdot E_g^{AlN} - b\cdot x\cdot(1-x)$$

We used the following constants[35,38] :

Band gap of GaN : $E_g^{GaN} = 3.42(eV)$

Band gap of AlN : $E_g^{AlN} = 6.2(eV)$

Bowing parameter : $b = 1.3(eV)$

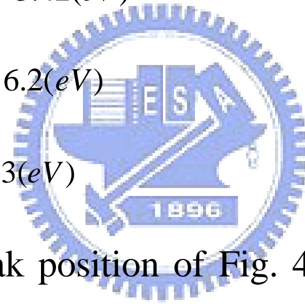

By plotting the PL peak position of Fig. 4-2-2 and Fig. 4-2-5 in Fig. 4-2-3 and Fig. 4-2-6, the peak position at 342 nm and 352 nm corresponds to an Al fraction of ~12.5% and ~6.5%, respectively.

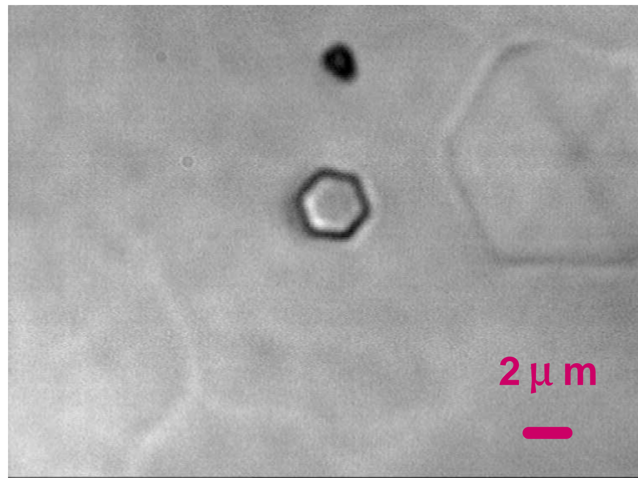

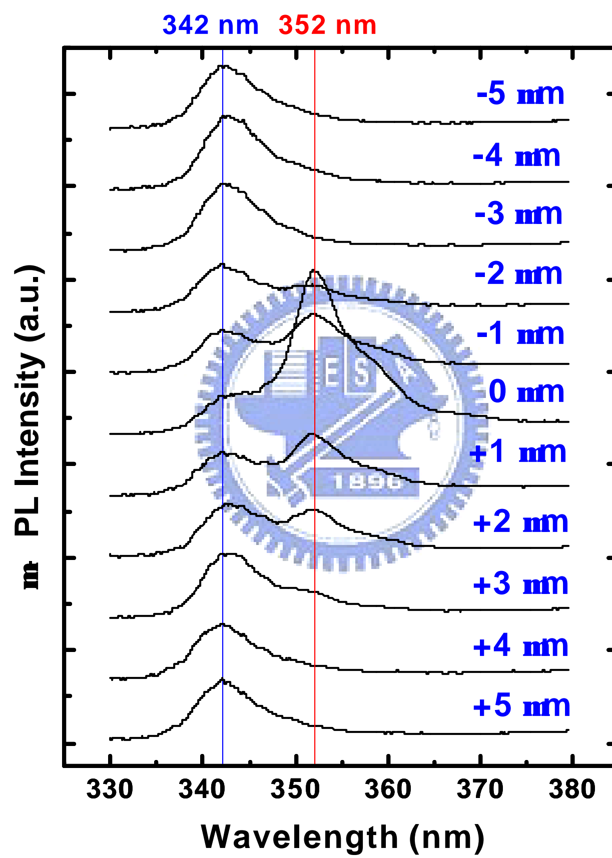

Fig. 4-2-1 and Fig. 4-2-2

Optical image and spatially resolved μ-PL spectra

of flat top hillock

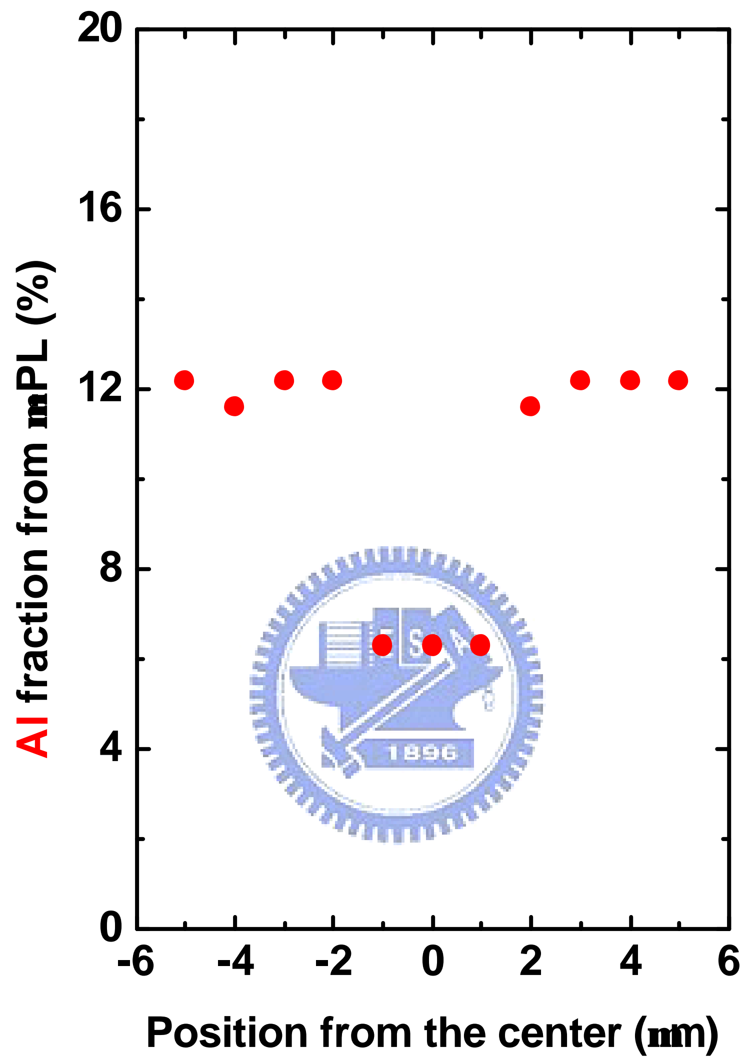

Fig. 4-2-3 Al fraction estimated from μ-PL spectra

（Flat Top hillocks）

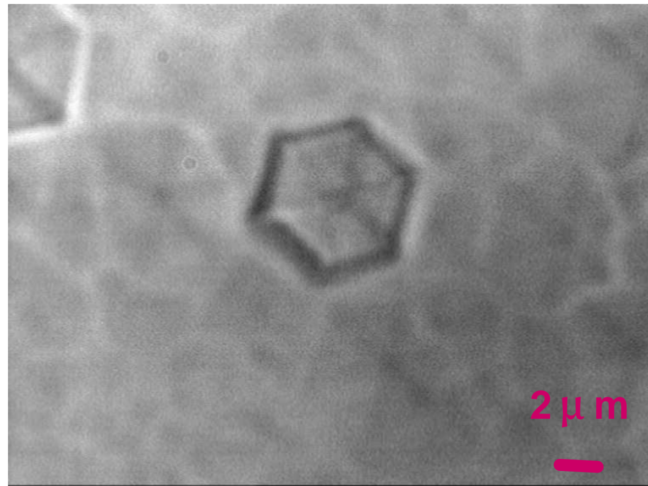

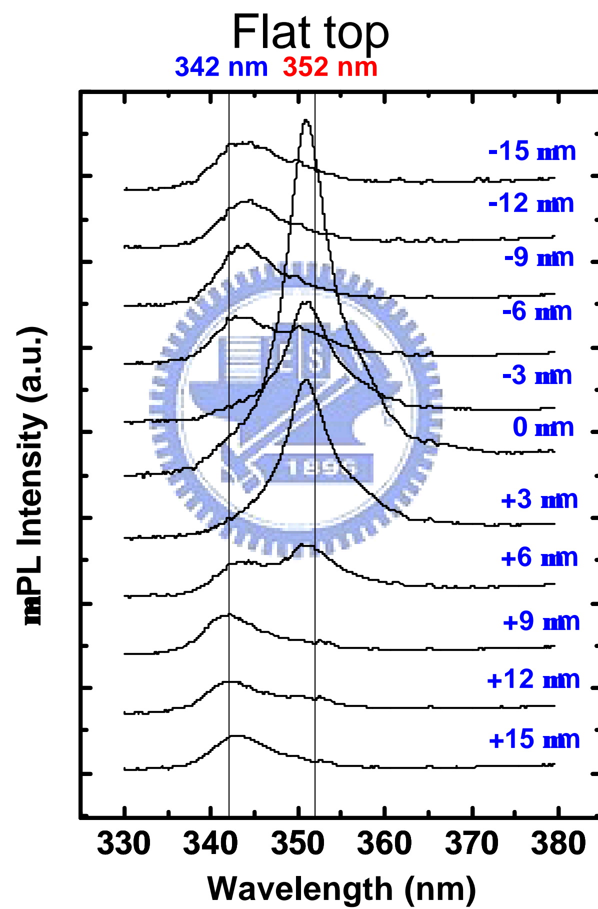

Fig. 4-2-4 and Fig. 4-2-5

Optical image and spatially resolved μ-PL spectra

of two steps hillocks

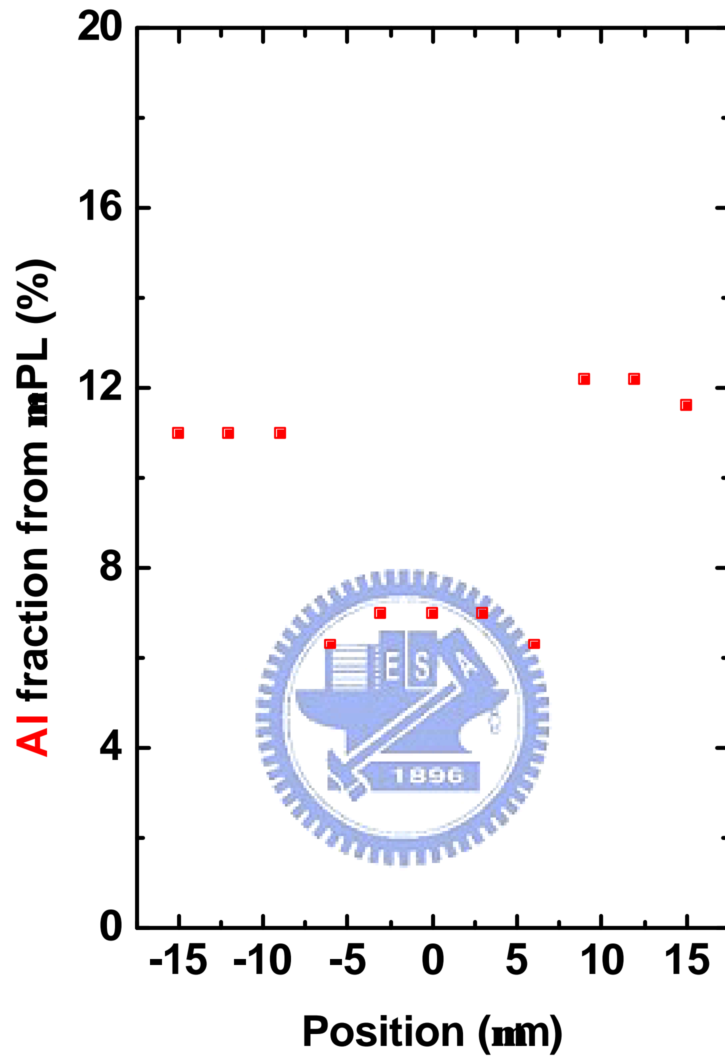

Fig. 4-2-6 Al fraction estimated from μ-PL spectra

（Two steps hillocks）

4-3 Micro-Raman spectra of hillocks

Besides the photoluminescence, we also used the μ-Raman scattering to investigate the distribution of the Raman modes. In Fig. 4-3-1 and Fig. 4-3-2, we show the optical image and spatially-resolved Raman spectra. In the plain region, the E_2 mode frequency is ~574 cm^{-1}, but it shifts toward ~570 cm^{-1} in both two types of hillocks. The full width at half maximum (FWHM) is ~ 6cm^{-1} in the plain region, and decreases to ~ 4.5 cm^{-1} inside the hillocks. According to the experimental results, the phonon frequency softening and FWHM reduction of the E_2 mode, may be attributed to the Al fraction variation.[32-33] In the Davydov *et al's* study[32], they indicated that the E_2 phonon frequency will increase monotonically with the Al fraction in $Al_xGa_{1-x}N$. The E_2 frequency of GaN and AlN is 567.6 cm^{-1} and 610 cm^{-1}, respectively[34,25]. By using a linear approximation:

$$E_2(Al_xGa_{1-x}N) = E_2(AlN) \times x + E_2(GaN) \times (1-x),$$

one may obtain the Al fraction. Since the E_2 phonon frequency in the flat region is ~574 cm^{-1} and ~570 cm^{-1} inside the hillocks, we estimated that the Al fraction in the flat region is ~ 8% but only ~4% inside the hillocks. In addition to the E_2 mode, we also observed another Raman peak at ~542 cm^{-1} inside the flat top hillock, but none in the two-step sidewall hillocks.

Flat Top Hillock

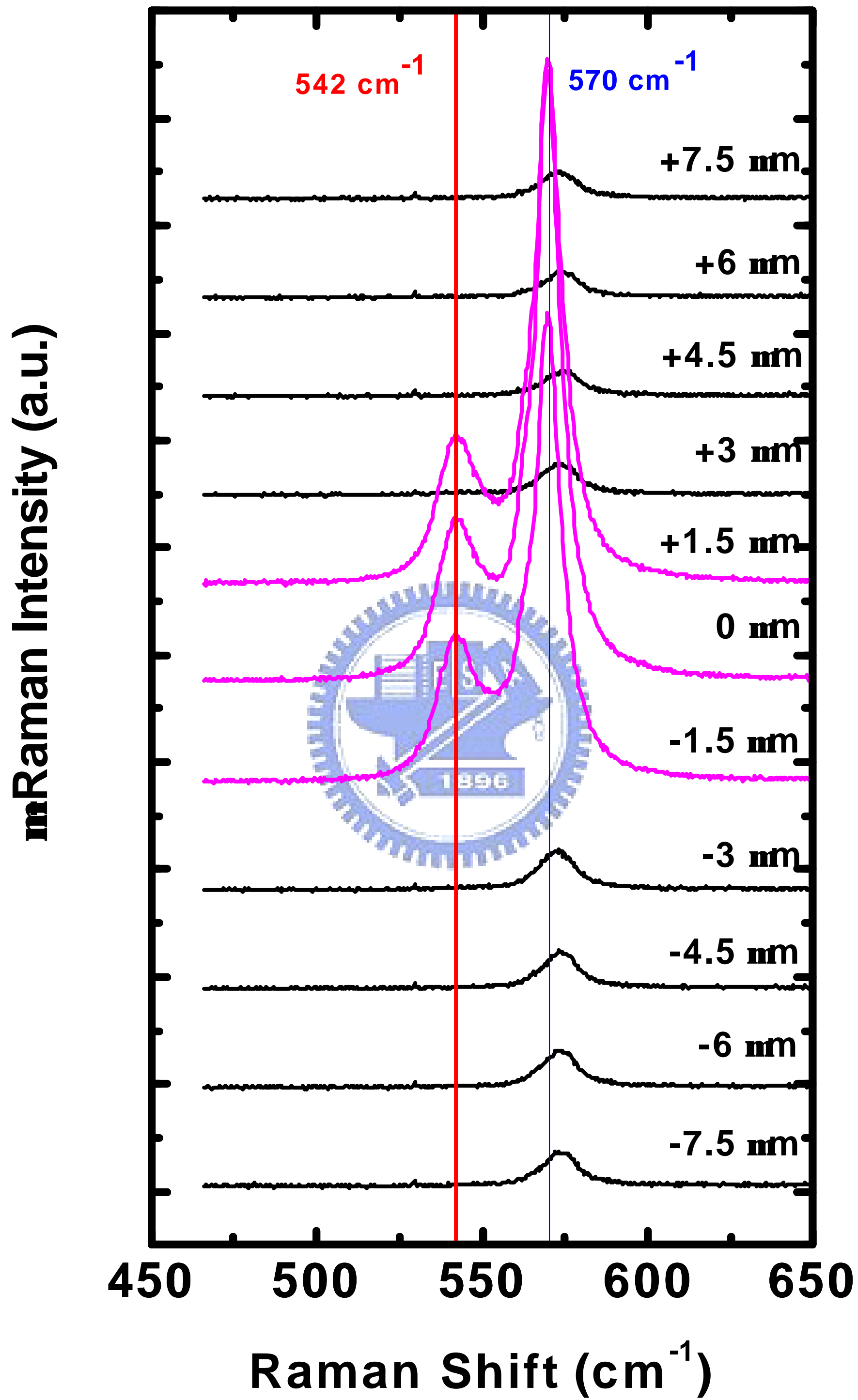

Fig. 4-3-1

Spatially resolved Raman spectra

Flat Top Hillock

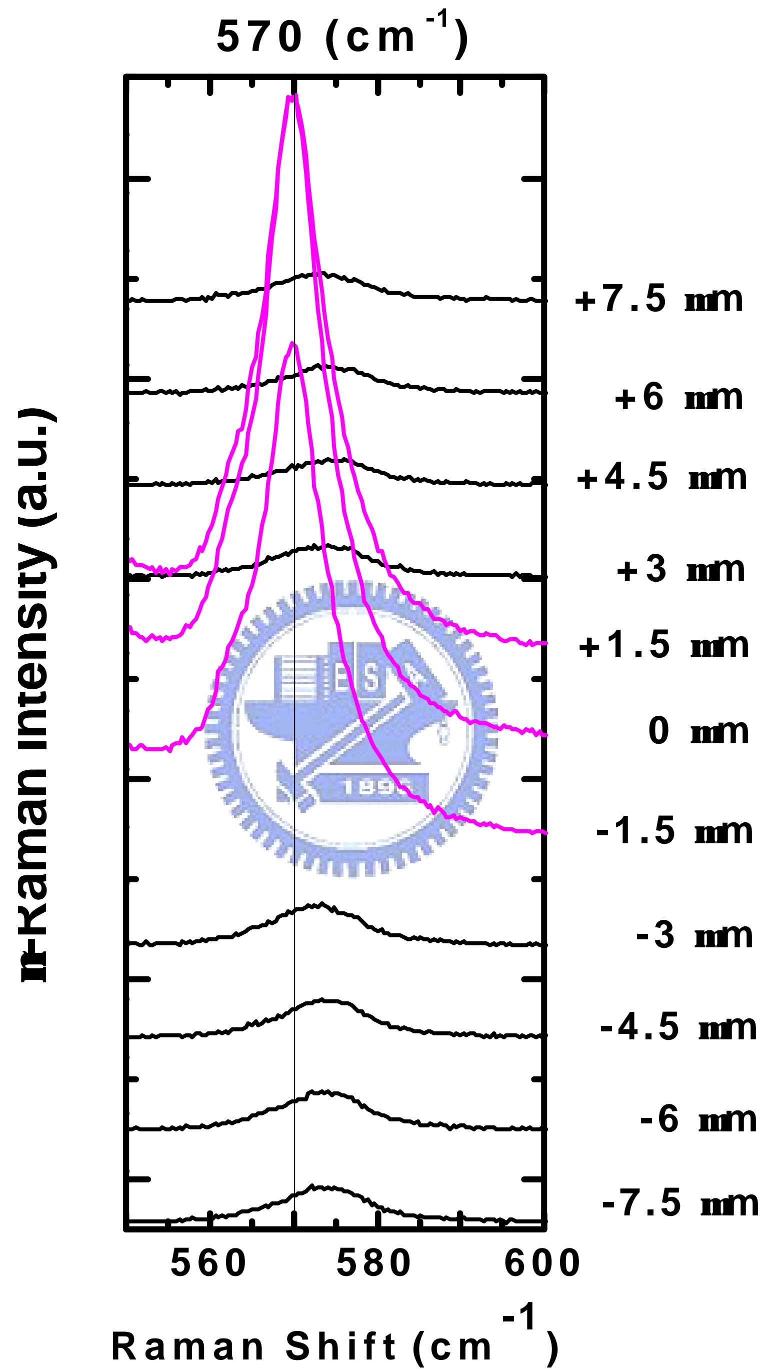

Magnified spectra of Fig. 4-3-1

（Between 550-600 cm^{-1}）

Flat Top Hillock

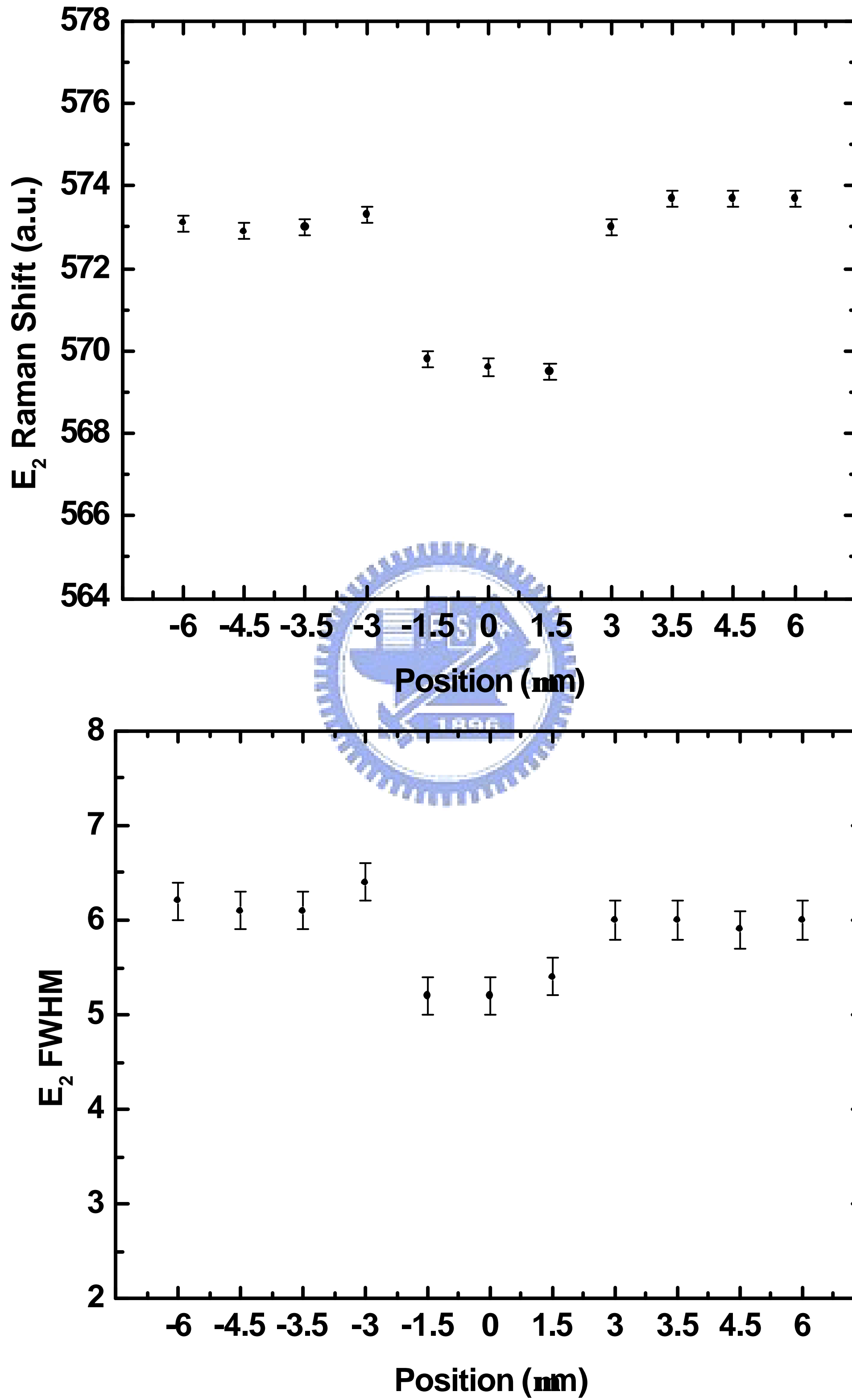

Spatially resolved E_2 Raman frequency and its FWHM

Two-Steps Hillock

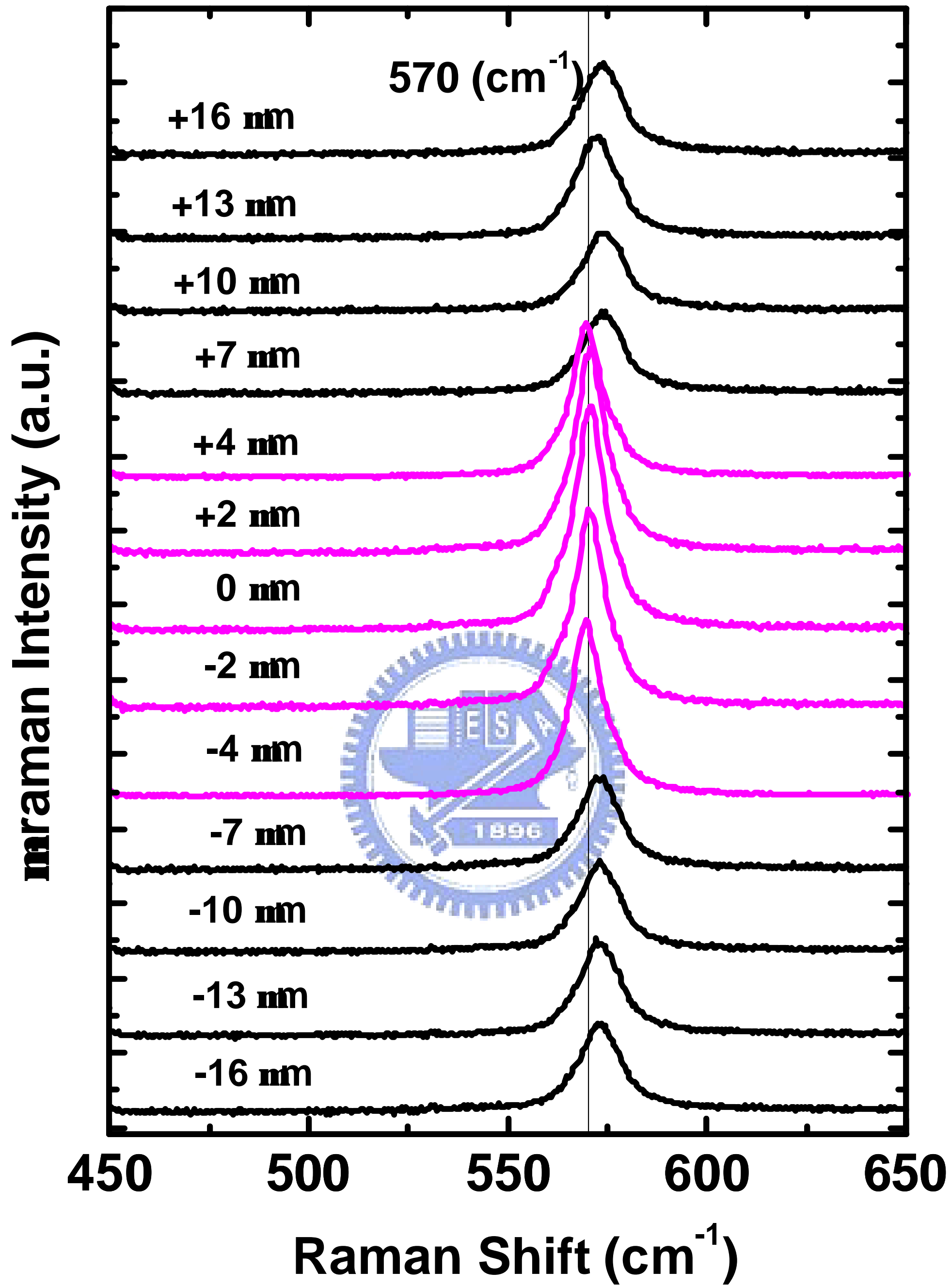

Fig. 4-3-2

Spatially resolved Raman spectra

Two-Steps Hillock

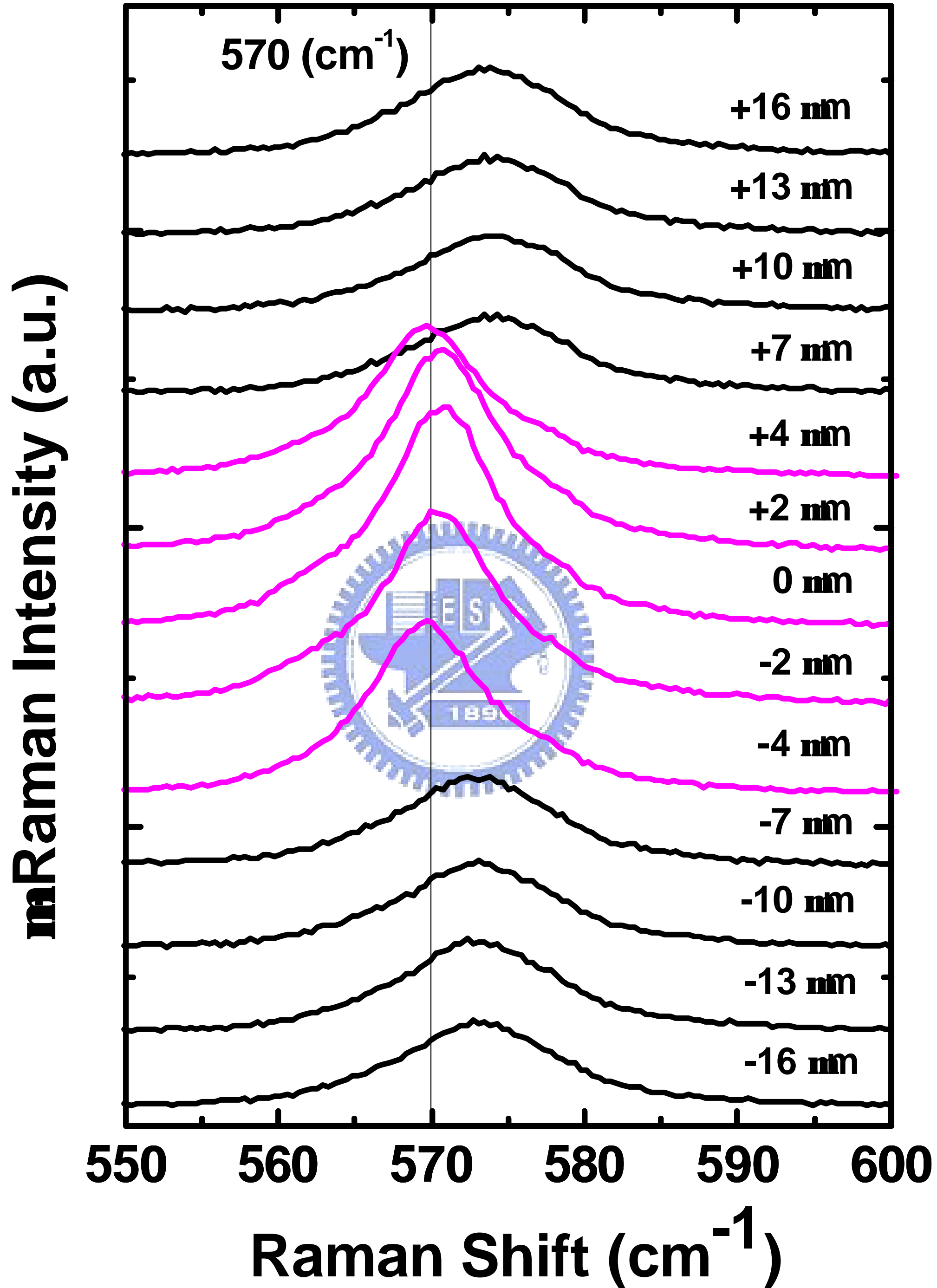

Magnified spectra of Fig. 4-3-2

(Between 550-600 cm^{-1})

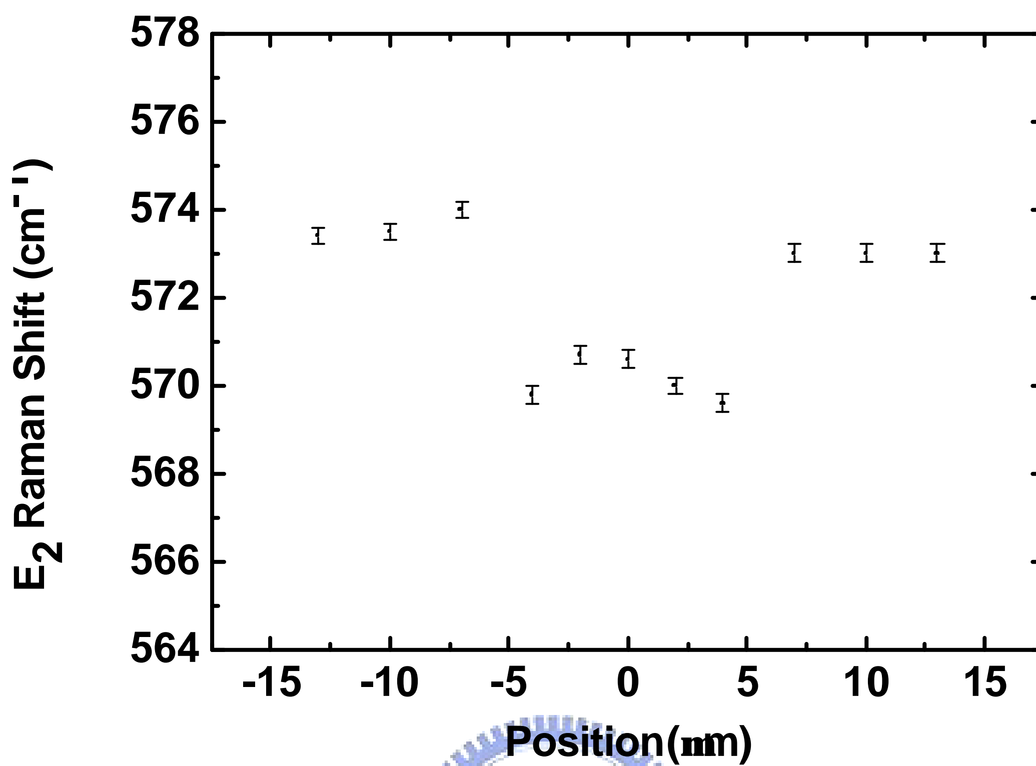

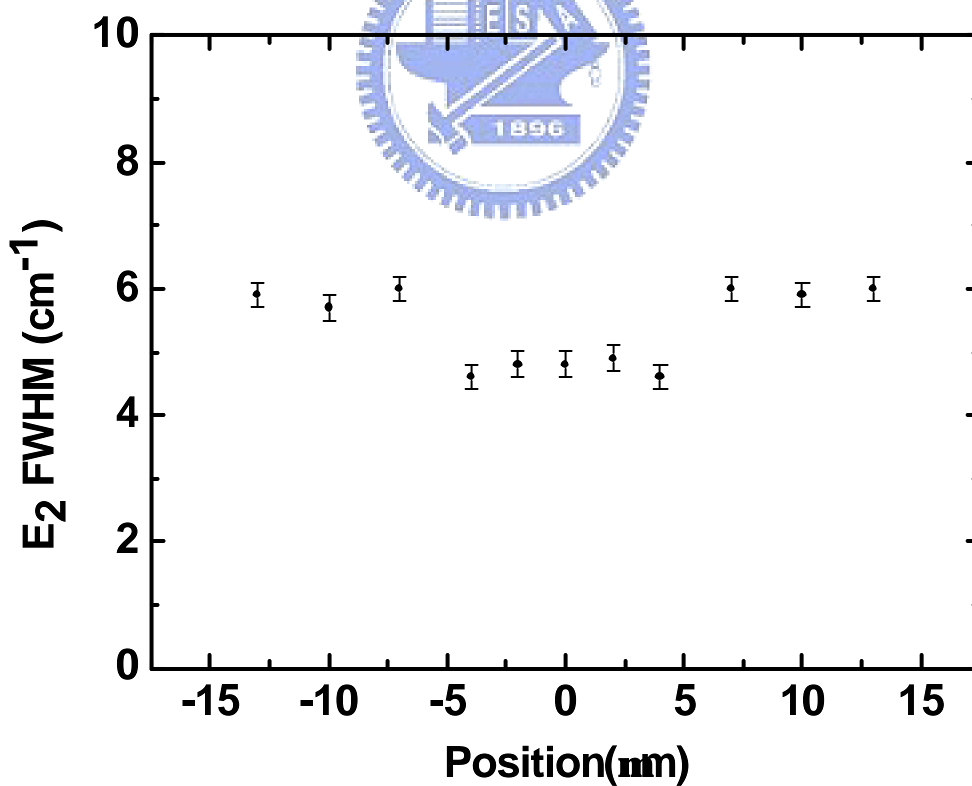

Spatially resolved E_2 Raman frequency and its FWHM

According to other studies, the additional peak near the E_2 mode may be due to the mixed crystal – such as cubic or hexagonal phase contributing to Raman signals[27]. In Liu *et al.*'s report[29], they found some surface irregularities on cubic GaN, and some of them exhibit both cubic TO mode (~552 cm^{-1}) and hexagonal A_1 (TO) (~530 cm^{-1}), E_2 (TO) (~560 cm^{-1}) from the μ-Raman measurements. They attributed the additional Raman signals to the hexagonal GaN sitting on or being embedded into the cubic GaN layer. Thus, they can observe the hexagonal GaN signals on cubic GaN. Besides the above suggestion, another possibility is that the forbidden Raman modes (A_1 (TO) or E_1 (TO)) appear in the $z(xx)\bar{z}$ scattering geometry. In Kuball *et al.'s* study[30], they have found the forbidden Raman signals in the window region of GaN ELO (Epitaxial Laterally Overgrown) structure. They proposed that the high-defect density in the windows region may breakdown the Raman selection rule, so that the forbidden Raman signals can occur. Hao *et al.* also observed the forbidden Raman signals on the ELO GaN structure at coalescence edges, they assigned the observation to the superposition of backscattering and right angle scattering from the coalescence edges. But in our studies, the forbidden Raman signals arise only in the flat top hillocks, but not in the two-step hillocks. Because the flat top hillocks do

not have the declining edge that assist scattering from different polarization Raman modes, and the two-steps hillock has declining edges, and yet no additional Raman signals were detected, they implied that the extra Raman peak can't result from the declining edge that brings about the right angle scattering. From the above discussion and Davydov *et al.*'s report[25], we suggest that this additional Raman peak at ~542 cm^{-1} is the A_1 (TO) mode that should only arise in the $y(zz)\bar{y}$ and $y(xx)\bar{y}$ scattering configurations.

By comparing the results in Figs. 4-3-3 and 4-3-4, the estimation of Al fraction from the E_2 Raman mode is lower than the results of PL spectra. Because the strain reflects the distance between the atoms, that eventually changes the phonon frequency, so does the E_2 peak position shifts, in the Raman measurements,

The strain may result from the doping of impurity, the thickness of thin film, cracks on the surface, or the composition fluctuation, *etc*. The composition fluctuation may be the main cause for the E_2 shift but other effects can't be completely ruled out, so that there is some discrepancy between the estimations from μ-PL and μ-Raman measurements.

4-4 EDX analysis of hillocks

In order to check our analyses from the μ-PL spectra and μ-Raman spectra, we utilized the X-ray micro analysis – EDX to analyze the Al fraction inside the hillock and on the plain region. In Fig. 4-5-1 and Fig. 4-5-2, we show the SEM images and element analysis of the flat top and two-step sidewall hillocks. The Al fraction is obtained from the ratio of integrated Al signals to the sum of Al and Ga signals:

$$\text{Al fraction (\%)} = \frac{Al(Integrated)}{Al(Integrated) + Ga(Integrated)}$$

The results show that Al fraction inside the hillock is about 5~6%, but about 13~14% on the plain region. O'Donnell *et al*[30] had observed the In and Ga fraction fluctuation on the hexagonal InGaN hillock-like structures and such fluctuation also caused changes in the CL emission line. They had also found that when the In fraction increases, the luminescence efficiency decreases. They claimed that the higher the In fraction is, the lower the emission efficiency can be found on the CL image. In our studies of μ-PL and EDX, because the lower Al-fraction structure (hillock) have stronger luminescence intensity from the μ-PL spectra, this implies that the more the Al fraction, the lower the emission efficiency.

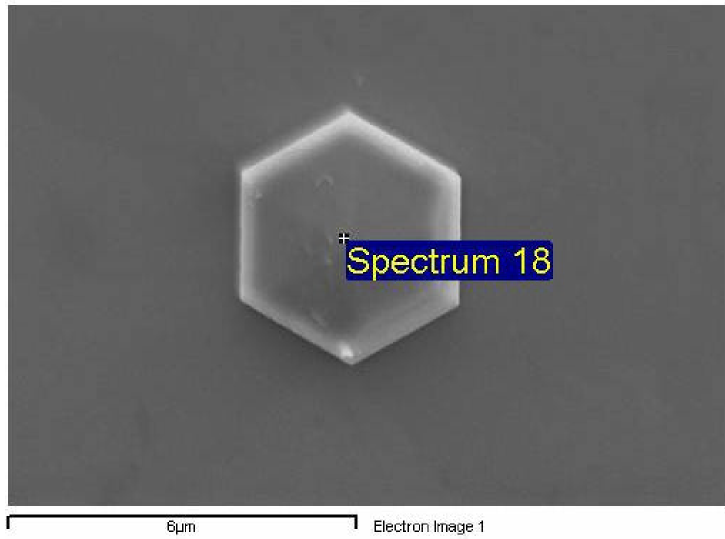

Al fraction from EDS (%)

20
16
12
8
4
0

-5.0 -2.5 0.0 2.5 5.0

Position (mm)

Fig. 4-5-1

Spatially resolved Al fraction of flat top hillock

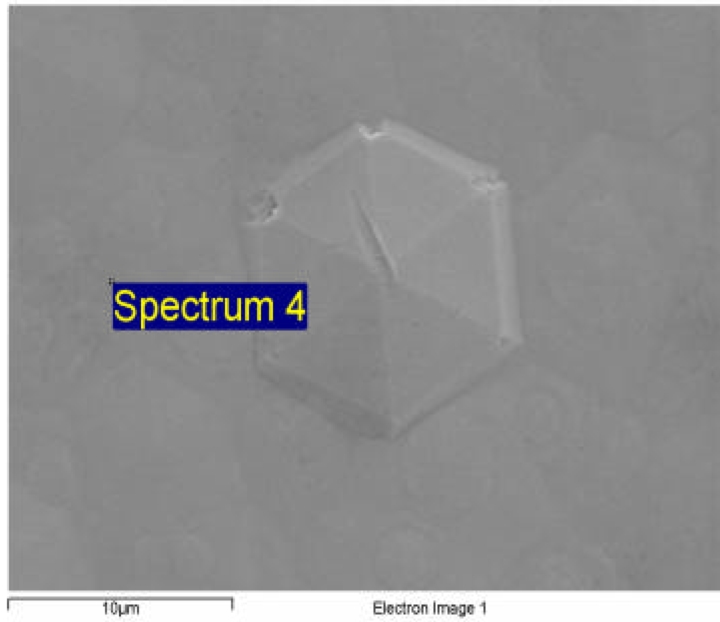

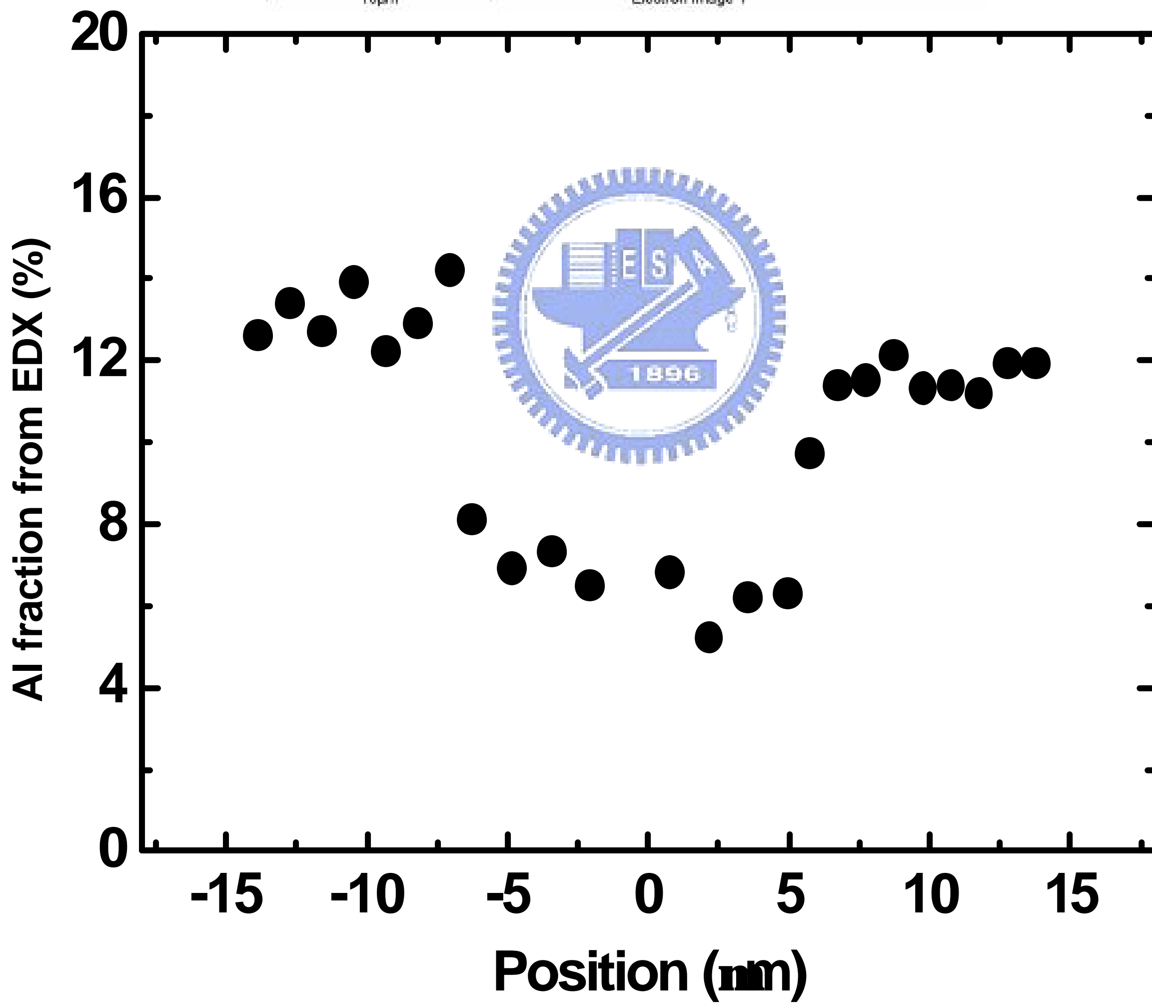

Fig. 4-5-2

Spatially resolved Al fraction of flat top hillock

This phenomenon can be observed both in K. P. O'Donnell and our studies. Similarly, SATO *et al.*[31] also reported that composition inhomogeneity on InGaN surface will contribute to different emissions in CL measurements. However, in L. H. Robins and D. K. Wickenden's study[17], they observed that the hexagonal hillock on $Al_xGa_{1-x}N$ had additional emission but did not give a clear explanation. Based on our measurements, the hillock itself is a low-Al-fraction structure, whether the flat top or the two step sidewall hillocks. Thus, the Stokes-like emission at ~350nm on hillocks is very likely due to the lower Al-composition-$Al_xGa_{1-x}N$.

Chapter 5 Conclusion

In this thesis, we had studied spontaneously formed hexagonal hillocks on the $Al_xGa_{1-x}N$ (x~0.12) thin film from the SEM images and the AFM profiles. We also utilized the μ-PL and the μ-Raman scattering to characterize the optical properties of hillocks. Besides, quantitative analysis on the hillocks by the EDX was also carriered out.

From the SEM images and the AFM profiles, two types of hillocks with different morphology were observed. The first type is a truncated hexagonal pyramid with a flat top. The angle between the side-wall and the flat region is about 55?, and the diameters of these hillocks are about 2~6 μm. The second type hillock looked like a canopy, it has two-step sidewall and an obtuse apex. The angle between the first sidewall and the flat region is about 20?, and the angle between the second sidewall and the first sidewall is about 13?.

In the μ-PL spectra, we found both two types of hillocks emitting strong luminescence line at (~350nm), that is red shifted by ~ 10nm with respect to the plain region emission (~340nm). In order to understand the transition mechanism of the Stokes-like emission, we performed the μ-Raman scattering. From the spectra of both hillocks, the E_2 mode Raman shift is about 570 cm^{-1} that is red shifted from that on the plain

region at 574 cm^{-1} by 4 cm^{-1}. The FWHM of E_2 mode is less than 5 cm^{-1} inside the hillocks but increases to 6 cm^{-1} in the plain region.

The softening of the E_2 Raman frequency and the reduction of FWHM implied that the composition of Al may be reduced. In addition to the E_2 Raman mode, another Raman feature at about 542 cm^{-1} appeared only in the flat top hillocks, that is likely the forbidden A_1 (TO) Raman mode. We believed that the orientation of the flat top hillocks may differ from the two-step sidewall hillocks, so that under the same scattering configuration, one exhibited the forbidden Raman mode but another did not.

In order to examine the hypothesis of composition fluctuation, we utilized the EDX to analyze the composition fraction of Al on the hillock structures. The EDX data indicated that Al fraction is about 6-7 % inside both types of hillocks, but about 12-13% in the plain region. The results agreed well with that from the μ-PL spectra but slightly higher than that from the Raman spectra. However, all the results show that the Al fraction is reduced inside the hillocks.

Reference

1. W. Qian, G. S. Rohrer, M. Skowronski, K. Doverspike, L. B. Rowland, and D. K. Gaskill, Appl. Phys. Lett. **67** 2284 (1995)
2. Wook Kim, Ö. Aktas, A. E. Botchkarev, A. Salvador, S. N. Mohammad, and H. Morkoç, J. Appl. Phys. **79** 7657 (1996)
3. F. A. Ponce, J. W. Steeds, C. D. Dyer and G. D. Pitt, Appl. Phys. Lett. **69** (1996)
4. M. Herrera Zaldivar, P. Fernandez, J. Piqueras, J. Appl. Phys. **83** 462 (1998)
5. T. H. Myers, L. S. Hirsch, L. T. Romano, and M. R. Richards-Babb, J. Vac. Sci. Technol. B **16** 2261 (1998)
6. M. Sumiya, K. Yoshimura, T. Ito, K. Ohtsuka, and S. Fuke, K. Mizuno, M. Yoshimoto, H. Koinuma, A. Ohtomo and M. Kawasaki, J. Appl. Phys. **88** 1158 (2000)
7. Koichi Tachibana, Takao Someya, Satomi Ishida, and Yasuhiko Arakawa, Appl. Phys. Lett. **76** 3212 (2000)
8. X. Li, P. W. Bohn, Jeongyong Kim, J. O. White, J. J. Coleman, Appl. Phys. Lett. **76** 3031 (2000)
9. Kyoyeo Lee, Keunho Auh, Jpn. J. Appl. Phys. 40 L 13 (2001)
10. W. Czarczyski, P. Kieszkowski, St. asisz, R. Paszkiewicz, M. Taczaa, Z. Znamirowski, and E. onierz, J. Vac. Sci. Technol. B **19** 47 (2001)
11. Yong-Hoon Cho, H. M. Kim, T. W. Kang, J. J. Song ,W. Yang, Appl. Phys. Lett. **80** 1141 (2002)
12. HockM. Ng, Nils G. Weimann and Aref Chowdhury, J. Appl. Phys. **94** 650 (2003)
13. J. Tersoff and R. M. Tromp, Phys. Rev. Lett. **70** 2782 (1993)
14. N. Moll, M. Scheffler and E. Pehike, Phys. Rev. B **58** 4566 (1998)
15. I. Daruka, J. Tersoff and A. –L Barabasi, Phys. Rev. Lett. **82** 2753 (1999)
16. L. G. Wang, P. Kratzer, N. Moll and M. Scheffler, Phys. Rev. B **62** 1897 (2000)
17. L. H. Robins, D. K. Wikenden, Appl. Phys. Lett. **71** 3841 (1997)
18. M.Herrera Zaldivar, P. Fernandez, and J. Piqueras, J. Appl. Phys. **83** 462 (1998)
19. F. A. Ponce, J. W. Steeds, C. D. Dyer and G. D. Pitt, Appl. Phys. Lett. **69** 2650 (1996)
20. M.Herrera Zaldivar, P. Fernandez, and J. Piqueras, J. Appl. Phys. **90** 1058 (2001)
21. Y. G. Cao, M. H. Xie, Y. Liu, Y. F. Ng, H. S. Wu, S. Y. Tong, Appl. Phys. Lett. **83** 5157 (2003)
22. D. Rudloff, T. Riemann, J. Christen, Q. K. K. Liu, A. Kaschner, A. Hoffmann, Ch. Thomsen, K. Vogeler, M. Diesselberg, S. Einfeldt, and

D. Hommel, Appl.Phys. Lett. **82** , 367 (2003)
23. S. Einfeldt, M. Dießelberg, H. Heinke, D. Hommel, D. Rudloff and J. Christen, R. F. Davis , J. Appl. Phys. 92,118 (2002)
24. **陳蔚宗 ,氮化鋁鎵薄膜表面** Hillock **缺陷之螢光研究 電子物理所碩士論文**(2003)
25. V. Yu. Davydov , I. N. Goncharuk , A. N. Smirnov, Phys. Rev. B **65** 125203 (2002)
26. Ming S. Liu , Les A. Bursill and Steven Prawer, J. Appl. Phys. **90** 1761 (2001)
27. Ming S. Liu, Steven Prawer, Les A. Bursill, D. J. As and R. Brenn, Appl. Phys. Lett. **78** 2658 (2001)
28. M. Kuball, M. Benyoucef, B. Beaumont and P. Gibart, J. Appl. Phys. **90** 3656 (2001)
29. S. Tripathy, S. J. Chua, M. S. Hao, E. K. Sia, A. Ramam, J. Zhang, W. H. Sun, and L. S. Wang, J. Appl. Phys. **91** 5840 (2002)
30. K.P. O'Donnell, P. G. Middelton, C. Trager-Cowan C. Young, S. C. Bayliss, I. Fletcher, W. Van der Stricht, I. Moerman, and P. Demeester, Appl. Phys. Lett. **73**, 3273 (1998)
31. Yoshio Yanase, Hideki Nishihata, Takashi Ochiai and Hideki Tsuya, Jpn. J. Appl. Phys. **37**, 1(1998)
32. V. Yu Davydov, I. N. Goncharuk, A. N. Smirnov, Phys. Rev. B **65,** 125203 (2002)
33. Ming S. Liu, Les A. Bursill and Steven Prawer, J. Appl. Phys. **90** 1761 (2001)
34. V. Yu. Davydov, I. N. Goncharuk, A. N. Smirnov, A. E. Nikolaev, W. V. Lundin, A. S. Usikov, A. A. Klochikhin, J. Aderhold, J. Graul, O. Semchinova, and H. Harima, Phys. Rev. B **65** 125203 (2002)
35. H. Angerer, D. Brunner, F. Freudenberg and O. Ambacher M. Stutzmann, R. Höpler, T. Metzger, E. Born G. Dollinger, A. Bergmaier, S. Karsch, and H.-J. Körner, Appl.Phys. Lett. **71** , 1504 (1997)
36. Ashcroft and Mermin, *Solid state physics* (Thomson Learning, Inc.)
37. M.R.H. Khan, Y. Koide, H. Itoh, N. Sawaki, and I. akasaki, Solid State Commun. **60**, 509 (1986)